Title
Seismicity and Stress Associated With a Fluid-Driven Fracture: Estimating the Evolving Geometry

Journal
Journal of Geophysical Research: Solid Earth, 125(12)

ISSN
2169-9313

Authors
Vasco, DW
Smith, J Torquil
Hoversten, G Michael

Publication Date
2020-12-01

DOI
10.1029/2020jb020190

Peer reviewed

Seismicity and stress associated with a fluid-driven fracture: Estimating the evolving geometry

D. W. Vasco [1], J. Torquil Smith [1], and G. Michael Hoversten [2]

[1]Energy Geosciences Division, Lawrence Berkeley National Laboratory, Berkeley, California.
[2]Chevron Energy Technology Company, San Ramon, California.

Key Points:

- Coupling poroelasticity and rate- and state-dependent friction provides a basis for relating fracture aperture changes and leak-off to microseismicity in the surrounding medium.
- Using the methodology we devise an inverse problem for imaging an evolving fracture.
- An application to the growth of a hydro-fracture highlights its heterogeneous development.

Corresponding author: D. W. Vasco, `dwvasco@lbl.gov`

Abstract

A coupled approach, combining the theory of rate- and state-dependent friction and methods from poroelasticity, forms the basis for a quantitative relationship between displacements and fluid leak-off from a growing fracture and changes in the rate of seismic events in the region surrounding the fracture. Poroelastic Green's functions link fracture aperture changes and fluid flow from the fracture to changes in the stress field and pore pressure in the adjacent formation. The theory of rate- and state-dependent friction provides a connection between Coulomb stress changes and variations in the rate of seismic events. Numerical modeling indicates that the Coulomb stress changes can vary significantly between formations with differing properties. The relationship between the seismicity rate changes and the changes in the formation stresses and fluid pressure is nonlinear, but a transformation produces a quantity that is linearly related to the aperture changes and fluid leak-off from the fracture. The methodology provides a means for mapping changes in seismicity into fracture aperture changes and to image an evolving fracture. An application to observed microseismicity associated with a hydro-fracture reveals asymmetric fracture propagation within two main zones, with extended propagation in the upper zone. The time-varying volume of the fracture agrees with the injected volume, given by the integration of rate changes at the injection well, providing validation of the estimated aperture changes.

1 Introduction

Fluid-driven fracturing is an important process in both the natural world, for example in magmatic fluid intrusion (Dvorak et al., 1986; Dieterich et al., 2000; Pedersen et al., 2007; Hamling et al., 2010; Shelly et al., 2013), and in industrial activities such as geothermal energy extraction (Albright & Pearson, 1982) and hydro-carbon exploitation (Eaton, 2018), and environmental remediation and waste disposal (McClain, 1971; Ajo-Franklin et al., 2012). The fracturing process itself is complicated and involves nonlinear interactions between the fluid flow within the fracture and the dynamics of fracture evolution (Detournay, 2004; Dahm et al., 2010; Zhou & Burbey, 2014; Yarushina et al., 2013). The literature on each of these aspects is vast, as is the amount of research on the coupled evolution of fractures. While there have been extensive numerical and laboratory studies of fracture initiation and evolution [see for example Bunger and Detournay (2008); Hoek and Martin (2014); Gordeliy and Peirce (2013)], there are few direct observations of fracture dynamics in a field setting. These measurements are essentially point observations obtained during fracture movement (Guglielmi, Cappa, et al., 2015). Thus, there is a need for imaging fracture evolution at the field scale.

Imaging the opening of a fracture is a difficult task due to the limited width of the feature, the rapid changes in properties, the significant depth of the event, and the complexity of the process, though there have been improvements in seismic imaging (Grechka et al., 2017). Much of the deformation within the fracture, and directly on the fracture surface, is aseismic or at frequencies that require broadband sensors (Tary et al., 2014; Guglielmi, Cappa, et al., 2015). One common feature of an opening fracture is an increase in the number of micro-seismic events in the surrounding region due to fluid flow and changes in the local stress field. This leads to changes in the rate of microseismicity around the fracture. Such fracture-related microseismicity is illustrated in Figure 1, where we plot events associated with the injection of fluid into a newly created hydro-fracture that was monitored using microseismicity. The events detected during the monitoring are from a field experiment that we will analyze in the Applications section below. The micro-seismic events resulting from the injection of fluid into the fracture were identified and located using 80 seismometers in four boreholes surrounding the injection well (Figure 1), as described in Vasco, Nakagawa, et al. (2019). There is also a temporal association between the developing microseismicity and the fluid pressure and aperture changes within

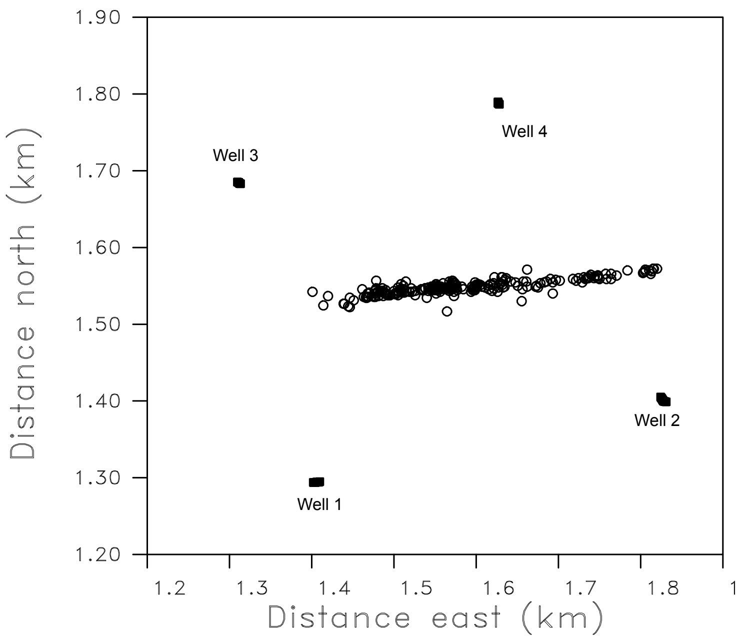

Figure 1. Plan view of the traces of the four wells used to monitor the microseismicity associated with the creation of a hydraulic fracture in the central region between the wells. The positions of the seismometers in each well are plotted in a local coordinate system as filled squares. Event epicenters, also plotted in the local coordinates, indicating a linear vertically planar feature.

the fracture. The progression of microseismicity contains useful information on the evolution of the fracture in space and time.

In examining the temporal variation in event location there is some evidence of migration to the east of the treatment well, which is located at 0.25 km in Figure 2, but there is considerable scatter and it is difficult to discern a coherent pattern. We can average the microseismicity over rectangular spatial bins, in order to better define the eastward migration of events from the injection well. In Figure 2 we have divided up the fracture zone into an 11 by 11 grid of bins, where each bin is a 54.5 m (x) by 18.2 m (z) patch. We bin all events located in that rectangular patch, adding all events that project down onto the patch from the out of plane direction. By examining the number of events in each 10 minute time increment, we can extract the temporal variation in the rate of events for each bin. The peak in the number of events appears later in time for bins that are farther from the injection well. In addition, the number of events appears to decrease with distance from the injection well, though there is an exception in going from bin (7,5) to bin (8,5). Thus, there are systematic changes in the rate of seismic events in both space and time. This suggests that one can use the changes in the rate of occurrence of microseismic events in the region surrounding the macroscopic hydro-fracture to better understand its evolution. That is, these rate changes are directly related to the evolution of the fracture. To date, the increased microseismicity has primarily been used to define qualitative features of stimulated fractures, such as their general geometry (Rutledge & Phillips, 2003). Such information is sufficiently important in evaluating hydro-fracture development that microseismic monitoring is increasingly common (Eaton, 2018). However, the temporal and spatial variations in microseismicity rates have not been used in a quantitative sense to image the detailed evolution of a fluid driven fracture in space and time. We discuss an approach utilizing ideas from rate and state-dependent failure

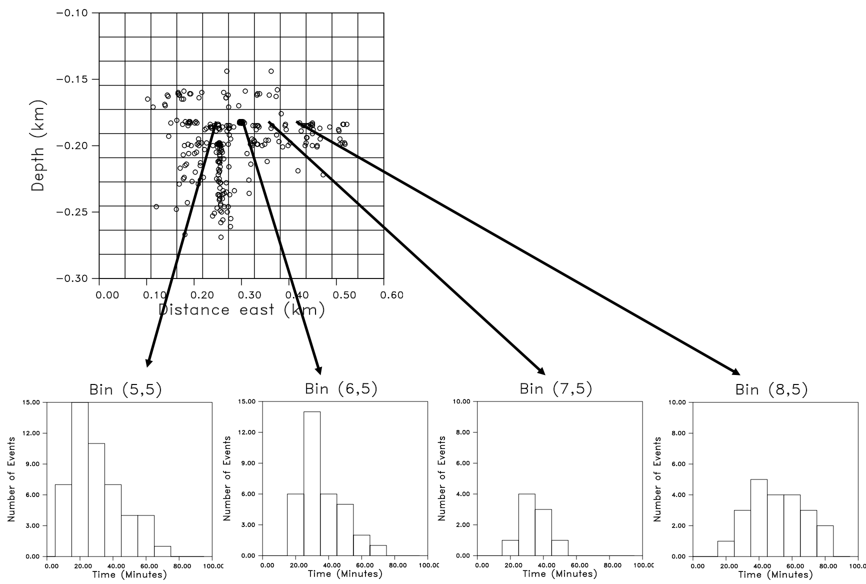

Figure 2. Histograms of microseismic events as a function of time for four patches of the 11 by 11 grid of cells encompassing the fracture.

and poroelasticity to develop a quantitative relationship between displacements and leak-off from a fluid filled fracture and changes in microseismicity in the region surrounding the fracture. The methodology provides a basis for an inverse problem whereby observed seismicity is used to infer aperture changes and fluid leak-off due to the opening of the fracture. We illustrate the technique with an application to a developing hydraulic fracture.

2 Methodology

2.1 Poroelastic Governing Equations, Green's Functions, Aperture Change, and Stress

While it has often been assumed that direct pore pressure changes govern the generation of microseismic events due to injection and fracturing (Shapiro et al., 2002), coupled porelasticity (Biot, 1941; Rice & Cleary, 1976; Segall, 1989; Wang, 2000; Pride, 2005) has been shown to provide an important contribution to the generation of microseismic events (Rozhko, 2010; Rutqvist et al., 2008, 2013; Segall & Lu, 2015; L. R. Johnson & Majer, 2017). In this section we develop a relationship between the aperture change on the fracture and associated fluid leak-off, and stress changes in the surrounding region, based upon theory of poroelasticity.

2.1.1 Governing Equations

Here we consider the equations governing the response of a poroelastic medium to an opening fracture. We consider a single fluid inhabiting the pores, though it is likely to be fluid mixture that we might have to model as an effective composite fluid. An al-

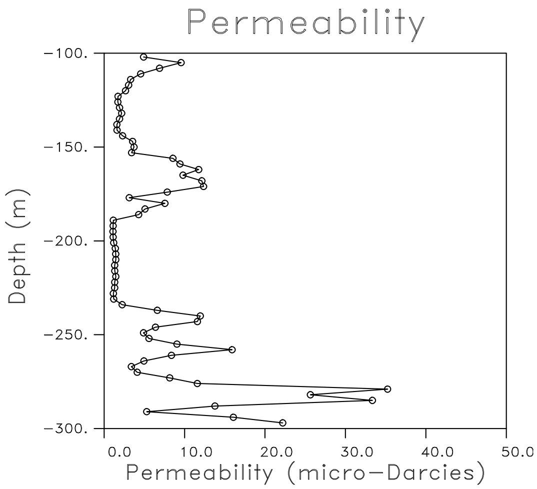

Figure 3. Permeability variation with depth, obtained from a log in the injection well.

ternative approach would be to adopt the recent extension of Biot theory to N_f fluids as in (Vasco, Alfi, et al., 2019) assuming small changes in saturation, allowing for a local linearization. Such an approach may be appropriate for our application, as the permeability is extremely low and the initial fluid leak-off is likely to be small prior to the generation of microseismic events around the hydro-fracture. Because fluid flow may be important at intermediate and longer time scales, we consider the case of a single pore fluid with no restrictions on the possible fluid flow. Our modeling is based upon the coupled equations of (Masson et al., 2006) and (Masson & Pride, 2011), whereby we neglect the creation of viscous boundary layers. Due to the dispersive nature of poroelastic propagation, it is most straight-forward to consider the governing equations in the frequency domain. This approach is generally valid for frequencies below about 10 kHz. We write the governing equations in terms of the displacement of the solid frame, $\mathbf{u}(\mathbf{x}, \omega)$, and the fluid displacement relative to the solid frame, $\mathbf{w}(\mathbf{x}, \omega) = \phi\,(\mathbf{u}_f - \mathbf{u})$,

$$\omega^2 \rho \mathbf{u} + \omega^2 \rho_f \mathbf{w} = -\nabla \cdot \mathbf{T} + \mathbf{s}(\Sigma) \tag{1}$$

$$\omega^2 \rho_f \mathbf{u} + i\omega \frac{\eta}{k} \mathbf{w} = \nabla p_f - \mathbf{f}(\Sigma) \tag{2}$$

where η is the fluid viscosity, $\mathbf{T}(\mathbf{x}, \omega)$ is the stress tensor, $p_f(\mathbf{x}, \omega)$ is the fluid pressure, ρ and ρ_f are the total and fluid densities, and $k(\mathbf{x}, \omega)$ is an integro-differential operator when expressed in the time domain [see (Pride, 2005)]. The functions $\mathbf{s}(\Sigma)$ and $\mathbf{f}(\Sigma)$ represent the driving forces that act at all points of the source Σ, which is the surface of the fracture. In our application these forces will be due to the displacement of the fracture walls and the fluid flow out of the fracture. The form of the frequency-dependent function $k(\mathbf{x}, \omega)$ is a variation of that given in D. L. Johnson et al. (1987),

$$\frac{1}{k(\mathbf{x}, \omega)} = \frac{1}{k_o(\mathbf{x})} \left[1 - i\omega \frac{\rho_f k_o(\mathbf{x})}{\eta \phi(\mathbf{x})} \right] \tag{3}$$

where $k_o(\mathbf{x})$ is the intrinsic permeability. For most seismic field data the dynamic variation is not significant and the permeability is dominated by $k_o(\mathbf{x})$. This quantity can vary by an order of magnitude or more, as shown by permeability log plotted in Figure 3. This figure displays the depth variation in the region around the fracture site plotted in Figure 1. The permeability of the host rock, which consists of various shale formations with mixtures of sand, is quite low.

In addition to the governing equations (1) and (2), there are two constitutive relationships connecting the stress tensor, $\mathbf{T}$, and the fluid pressure, P_f, to the strains and fluid volume changes,

$$\mathbf{T} = \boldsymbol{\mathcal{A}} : \nabla\mathbf{u} + \mathcal{C}\nabla\cdot\mathbf{w} \tag{4}$$
$$-P_f = \boldsymbol{\mathcal{C}} : \nabla\mathbf{u} + M\nabla\cdot\mathbf{w}, \tag{5}$$

(Pride & Haartsen, 1996). The quantity $\boldsymbol{\mathcal{A}}$ is a fourth-order stiffness tensor that has the representation

$$\boldsymbol{\mathcal{A}} = \mathcal{A}_{ijkl}\mathbf{e}_i\mathbf{e}_j\mathbf{e}_k\mathbf{e}_l \tag{6}$$

where $\mathbf{e}_i$ is the unit vector along the i-th coordinate axis. The coefficients $\mathcal{A}_{ijkl}$ of the tensor obey the material symmetries noted in (Pride & Haartsen, 1996) resulting in 21 independent parameters in the representation of $\boldsymbol{\mathcal{A}}$. We have used the symmetries of $\boldsymbol{\mathcal{A}}$ to write $\boldsymbol{\mathcal{A}} : \left[\nabla\mathbf{u} + \nabla\mathbf{u}^T\right]/2$ as $\boldsymbol{\mathcal{A}} : \nabla\mathbf{u}$ in equation (4). For medium containing no fluids and described entirely by classical elasticity, one has

$$\boldsymbol{\mathcal{A}} = c_{ijkl}\mathbf{e}_i\mathbf{e}_j\mathbf{e}_k\mathbf{e}_l \tag{7}$$

where c_{ijkl} are the parameters generalizing Hooke's law for an anisotropic medium (Aki & Richards, 1980). For an isotropic poroelastic medium the tensor $\boldsymbol{\mathcal{A}}$ reduces to

$$\boldsymbol{\mathcal{A}} = \left[(H-2\mu)\,\delta_{ij}\delta_{kl} + \mu\left(\delta_{il}\delta_{jk} + \delta_{ik}\delta_{jl}\right)\right]\mathbf{e}_i\mathbf{e}_j\mathbf{e}_k\mathbf{e}_l \tag{8}$$

where $H = K_u + 4/3\mu$ is the undrained compressional wave modulus given in terms of the shear modulus μ and undrained bulk modulus K_u and discussed in (Pride, 2005). In an isotropic porous medium

$$\boldsymbol{\mathcal{C}} = C\mathbf{I} \tag{9}$$

where C is Biot's coupling modulus (Biot, 1962) and $\mathbf{I}$ is the identity matrix, and $\boldsymbol{\mathcal{C}} : \nabla\mathbf{u} = C\nabla\cdot\mathbf{u}$. The modulus M in equation (5) is the fluid-storage coefficient (Pride, 2005), a measure of the fluid volume change due to a fluid pressure change for a fixed sample size.

For the hydro-fracture experiment that we will consider later in this paper, the elastic properties were obtained from extensive well logs that were run in the injection well. The vertical variation in the compressional wave velocity observed in the well log was averaged over depth intervals and used to construct a layered model for the medium surrounding the hydro-fracture (Figure 4). It is evident that the elastic properties vary significantly with depth in this region, with changes in compressional velocity approaching 30%.

2.1.2 Green's Functions, Aperture Change, and Stress

In order to represent the displacements, and consequently the stresses, in terms of aperture change and fluid emanating from an evolving fracture, we shall need the Green's tensors that constitute the response of the poroelastic medium to impulsive sources (Burridge & Vargas, 1979; Norris, 1994; Pride & Haartsen, 1996; Karpfinger et al., 2009). Because poroelastic processes are characterized by two dependent fields, $\mathbf{u}(\mathbf{x},\omega)$ and $\mathbf{w}(\mathbf{x},\omega)$ one can have at least two distinct types of sources, one due to displacements and one due to fluid flow. We will denote the two classes of sources by the super-scripts u and w respectively. Therefore, in calculating the displacement Green's function we use the source

$$\mathbf{s}^u(\mathbf{x}) = \mathbf{d}^u\delta\left(\mathbf{x}-\mathbf{x}'\right) \tag{10}$$
$$\mathbf{f}^u(\mathbf{x}) = \mathbf{0} \tag{11}$$

while for the fluid source we have

$$\mathbf{s}^w(\mathbf{x}) = \mathbf{0} \tag{12}$$
$$\mathbf{f}^w(\mathbf{x}) = \mathbf{d}^w\delta\left(\mathbf{x}-\mathbf{x}'\right). \tag{13}$$

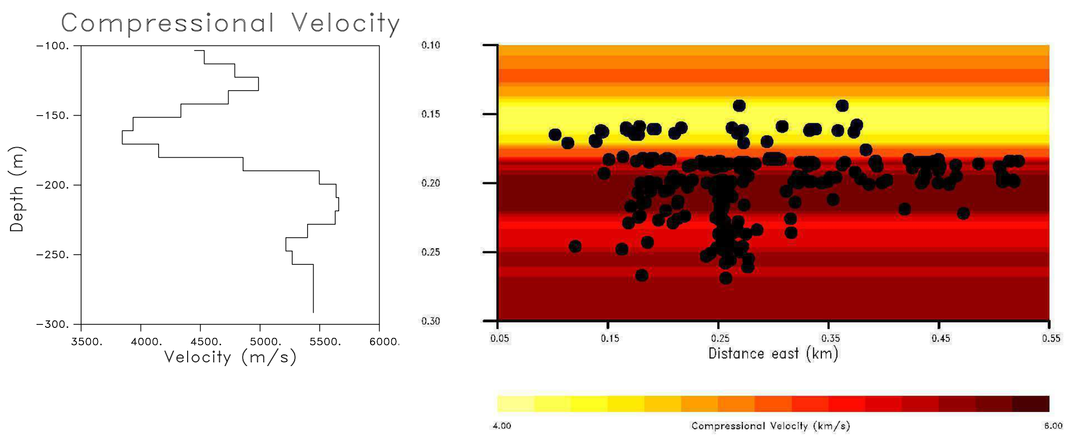

Figure 4. (Left panel) Vertical variation of the seismic compressional velocity obtained from well logs in the region under study. (Right panel) The background colors indicate the compressional velocity while the filled circles indicate the locations of observed microseismic events.

The three columns of the Green's tensors, which may be considered to be 3×3 matrices, are the fields corresponding to $\mathbf{u}(\mathbf{x},\omega)$ and $\mathbf{w}(\mathbf{x},\omega)$ for impulsive sources at $\mathbf{x}'$, denoted by $\mathbf{G}_u^\xi(\mathbf{x}|\mathbf{x}')$ and $\mathbf{G}_w^\xi(\mathbf{x}|\mathbf{x}')$, where the sources are directed along the three independent coordinate directions (Pride & Haartsen, 1996). We can construct the Green's tensors numerically using the finite-difference code noted above. That is, equations (1) and (2) can be solved using the finite-difference scheme presented in Masson et al. (2006) and Masson and Pride (2011). As in Pride and Haartsen (1996) we denote the vector fields associated with the two source types as $\mathbf{u}^\xi$ and $\mathbf{w}^\xi$, where $\xi = u$ or w depending on the source type. Similarly, we will have the associated solid stress tensors $\mathbf{T}^\xi$ and the fluid pressures P_f^ξ. The fundamental solutions, where the impulse may be directed along the arbitrary direction $\mathbf{d}^\xi$, are given in terms of the Green's tensors projected along the vectors

$$\begin{aligned}\mathbf{u}^\xi\left(\mathbf{x}|\mathbf{x}';\mathbf{d}^\xi\right) &= \mathbf{G}_u^\xi(\mathbf{x}|\mathbf{x}')\cdot\mathbf{d}^\xi && (14)\\ \mathbf{w}^\xi\left(\mathbf{x}|\mathbf{x}';\mathbf{d}^\xi\right) &= \mathbf{G}_w^\xi(\mathbf{x}|\mathbf{x}')\cdot\mathbf{d}^\xi. && (15)\end{aligned}$$

Note that there are four Green's tensors associated with the two types of sources and the two fields $\mathbf{u}$ and $\mathbf{w}$. If we substitute these expressions for $\mathbf{u}^\xi$ and $\mathbf{w}^\xi$ into equations (4) and (5), making use of the fact that $\mathbf{d}^\xi$ is constant in space, we can define the third-order Green's stress tensor $\mathbf{T}^\xi$ and the Green's fluid-pressure vector $\mathbf{P}^\xi$

$$\begin{aligned}\mathbf{T}^\xi &= \boldsymbol{\mathcal{A}}:\nabla\mathbf{G}_u^\xi+\mathcal{C}\nabla\cdot\mathbf{G}_w^\xi && (16)\\ -\mathbf{P}^\xi &= \boldsymbol{\mathcal{C}}:\nabla\mathbf{G}_u^\xi+M\nabla\cdot\mathbf{G}_w^\xi. && (17)\end{aligned}$$

Because the Green's tensors may be thought of as matrices rather than vectors, the Green's solid stress $\mathbf{T}^\xi$ is a third order tensor and the Green's fluid pressure $\mathbf{P}^\xi$ is a vector and not a scalar. Therefore, contracting these expressions with a vector, such as $\mathbf{d}^\xi$, will produce the appropriate second-order stress tensor and a scalar pressure.

Following the approach of Gangi (1970), where reciprocity is used to derive the representation theorem, Pride and Haartsen (1996) arrive at a general representation of $\mathbf{u}(\mathbf{x},\omega)$ and $\mathbf{w}(\mathbf{x},\omega)$ in terms of forces, tractions, and displacements distributed over a source volume and a source surface. Their representation generalizes that of an isotropic elastic medium, as presented in Burridge and Knopoff (1964), to a poroelastic medium. For the opening fracture of interest to us, we shall only need a subset of the terms in the general formulation of Pride and Haartsen (1996). As noted by Aki and Richards (1980), the statement of reciprocity follows from Betti's theorem and makes used of the symmetry of the stress tensor. The expression of reciprocity in a poroelastic medium that we shall need

$$\begin{aligned}&\int_\Sigma \mathbf{n}\cdot\{\mathbf{T}_2\cdot\mathbf{u}_1-\mathbf{T}_1\cdot\mathbf{u}_2-P_2\mathbf{w}_1+P_1\mathbf{w}_2\}\,d\Sigma\\ &\qquad=\int_V\{\mathbf{u}_2\cdot\mathbf{s}_1-\mathbf{u}_1\cdot\mathbf{s}_2+\mathbf{w}_2\cdot\mathbf{f}_1-\mathbf{w}_1\cdot\mathbf{f}_2\}\,dV \qquad (18)\end{aligned}$$

follows from the more general statement given in Pride and Haartsen (1996) for electroseismic waves. In our use of equation (18) we will only consider surface displacements and flows and we will neglect volume sources. If we specify that the quantities associated with the subscript 1 are the unknown fields $\mathbf{u}(\mathbf{x},\omega)$, and $\mathbf{w}(\mathbf{x},\omega)$, while the fundamental solutions generated by the point sources correspond to the fields with the subscript 2, then equation (18) produces the representation

$$\mathbf{d}^\xi\cdot\mathbf{X}_\xi=-\int_\Sigma\mathbf{n}\cdot\left\{\mathbf{T}^\xi\cdot\mathbf{u}-\mathbf{T}\cdot\mathbf{u}^\xi-p^\xi\mathbf{w}+p\mathbf{w}^\xi\right\}d\Sigma \qquad (19)$$

where $\mathbf{X}_u=\mathbf{u}$ and $\mathbf{X}_w=\mathbf{w}$ and we have neglected volume sources.

Now consider a source of displacements and fluid flow across an internal surface in the volume V, specifically across the fracture surface with a total area denoted by Σ.

We will consider displacements imposed on the fracture walls due to it's opening, as well as fluid flow across the fracture surfaces. As in Kennett (1983) and Aki and Richards (1980) the source Σ will consist of two closely-spaced surfaces, Σ^+ and Σ^-. In the case of an evolving fracture the surfaces are moving apart and fluid is flowing into the formation. Furthermore, there may also be shear displacements, leading to a component of the displacement discontinuity parallel to the fracture. If the fracture cuts a formation at an angle there may be flow that is not perpendicular to the fracture walls. Thus, we will consider general displacement and fluid flow discontinuities between the surfaces, which we denote by $[\mathbf{u}]$ and $[\mathbf{w}]$. Because we are only considering surface sources on Σ, and discontinuities in displacement and flow and not in traction or pressure, we are led to the representations

$$\mathbf{u}(\mathbf{x},\omega) = -\int_{\Sigma} \mathbf{n} \cdot \{\boldsymbol{\mathcal{A}} : \nabla \mathbf{G}_u^u + \mathcal{C}\nabla \cdot \mathbf{G}_w^u\} \cdot [\mathbf{u}]\, d\Sigma$$

$$+ \int_{\Sigma} \{\boldsymbol{\mathcal{C}} : \nabla \mathbf{G}_u^u \mathbf{n} + M\nabla \cdot \mathbf{G}_w^u \mathbf{n}\} \cdot [\mathbf{w}]\, d\Sigma \tag{20}$$

and

$$\mathbf{w}(\mathbf{x},\omega) = -\int_{\Sigma} \mathbf{n} \cdot \{\boldsymbol{\mathcal{A}} : \nabla \mathbf{G}_u^w + \mathcal{C}\nabla \cdot \mathbf{G}_w^w\} \cdot [\mathbf{u}]\, d\Sigma$$

$$+ \int_{\Sigma} \{\boldsymbol{\mathcal{C}} : \nabla \mathbf{G}_u^w \mathbf{n} + M\nabla \cdot \mathbf{G}_w^w \mathbf{n}\} \cdot [\mathbf{w}]\, d\Sigma. \tag{21}$$

These equations relate the displacement and flow at a point $\mathbf{x}$ in the medium, outside of the fracture, to sources of displacement and flow at a location $\mathbf{x}'$ on the fracture surface Σ. Note the differences between our expressions for a source distribution on an internal surface and the representation of poroelastic volume sources given by Karpfinger et al. (2009). Equations (20) and (21) are generalizations of the representations for an elastic medium, as given in Aki and Richards (1980), to those for a poroelastic medium. We can write equations (20) and (21) more succinctly as

$$\mathbf{u}(\mathbf{x},\omega) = -\int_{\Sigma} \mathbf{y}_u^u(\mathbf{x}|\mathbf{x}') \cdot [\mathbf{u}]\, d\Sigma + \int_{\Sigma} \mathbf{y}_w^u(\mathbf{x}|\mathbf{x}') \cdot [\mathbf{w}]\, d\Sigma, \tag{22}$$

$$\mathbf{w}(\mathbf{x},\omega) = \int_{\Sigma} \mathbf{y}_u^w(\mathbf{x}|\mathbf{x}') \cdot [\mathbf{u}]\, d\Sigma + \int_{\Sigma} \mathbf{y}_w^w(\mathbf{x}|\mathbf{x}') \cdot [\mathbf{w}]\, d\Sigma. \tag{23}$$

if we define the components of the integrand, such as $\mathbf{y}_u^u(\mathbf{x}|\mathbf{x}')$, in terms of the Green's function contributions,

$$\mathbf{y}_u^u(\mathbf{x}|\mathbf{x}') = \mathbf{n} \cdot \{\boldsymbol{\mathcal{A}} : \nabla \mathbf{G}_u^u + \mathcal{C}\nabla \cdot \mathbf{G}_w^u\} \tag{24}$$

and similarly for $\mathbf{y}_w^u(\mathbf{x}|\mathbf{x}')$, $\mathbf{y}_u^w(\mathbf{x}|\mathbf{x}')$, and $\mathbf{y}_w^w(\mathbf{x}|\mathbf{x}')$. Expressions for the stress and pressure changes in the region surrounding the fracture can be written in terms of the displacements and fluid flow across the fracture surfaces. Specifically, we begin with the integral representations (20) and (21) of the displacement and Darcy filtration velocity at a point $\mathbf{x}$ outside of the fracture. We can substitute these integral forms into the equations for the stress tensor and the fluid pressure, given by equations (6) and (7), to produce expressions for $\mathbf{T}(\mathbf{x},\omega)$ and $P_f(\mathbf{x},\omega)$ in terms of $[\mathbf{u}]$ and $[\mathbf{w}]$ on the fracture surface Σ. This representation is central to our formulation of the inverse problem discussed in the next sub-section. The aperture changes on the fracture are the components of $[\mathbf{u}]$ normal to the fracture surfaces. For a fracture surface oriented perpendicular to the direction of minimum stress there may not be shear along the fault and the entire displacement discontinuity could be associated with aperture change.

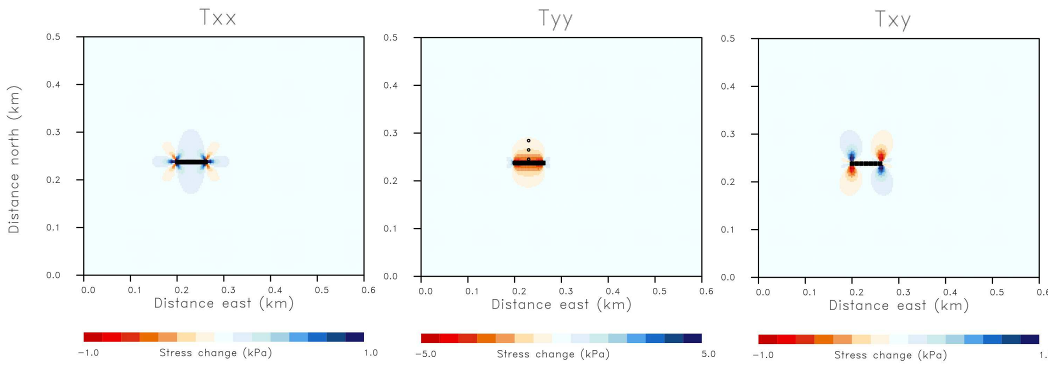

Figure 5. Spatial distribution of stress components in a horizontal plane cutting across a vertical fracture patch. The fracture is indicated by the black rectangle and is opening in the y direction. The stress changes are associated with an aperture change of 1 cm and a fluid pressure of 33 MPa within the fracture.

2.2 Formulation of the Inverse Problem

2.2.1 Relating Fracture Displacements and Leak-off to Stress and Fluid Pressure Changes in the Surrounding Medium

For the inverse problem we will use the developing seismicity around the hydrofracture to infer the geometry of the evolving fluid-driven fracture. Our first task will be to re-formulate the inverse problem into a discrete one by considering displacements and flow on rectangular sub-patches of the fracture plane. For example, we can consider the rectangular patches used in Figure 2 to bin the seismicity. Figure 5 displays a horizontal slice through the changes to three components of the stress field (T_{xx}, T_{yy}, and T_{xy}), caused by a linear aperture change distributed over the vertical patch. In addition, we include fluid leak-off associated with a constant pressure of 33 MPa within the fracture patch. We can integrate the functions $\mathbf{y}_u^u(\mathbf{x}|\mathbf{x}')$, $\mathbf{y}_w^u(\mathbf{x}|\mathbf{x}')$, $\mathbf{y}_u^w(\mathbf{x}|\mathbf{x}')$, and $\mathbf{y}_w^w(\mathbf{x}|\mathbf{x}')$ over the n-th sub-patch to get the total influence of the changes on the patch. For example, we can define the total response due to $\mathbf{y}_u^u(\mathbf{x}|\mathbf{x}')$ on the patch R_n,

$$\mathbf{Y}_n^{uu}(\mathbf{x}) = \int_{R_n} \mathbf{y}_u^u(\mathbf{x}|\mathbf{x}')\, d\mathbf{x}', \tag{25}$$

and similarly for $\mathbf{Y}_n^{uw}(\mathbf{x})$, $\mathbf{Y}_n^{wu}(\mathbf{x})$, and $\mathbf{Y}_n^{ww}(\mathbf{x})$. The complete response at a point $\mathbf{x}$ will be a linear sum over all of N the patches comprising the fracture surface. Each patch is assumed to undergo a displacement discontinuity $[\mathbf{u}_n]$ that may contain both shear and normal components. In addition, there will be the poroelastic response due to the fluid migration out of the fracture due leak-off. The pressure change due to this fluid migration and due to the stress changes induced by the fracture aperture changes are shown in Figure 6.

We can use the representations of $\mathbf{u}(\mathbf{x},\omega)$ and $\mathbf{w}(\mathbf{x},\omega)$ as a linear sum of the four functions $\mathbf{Y}_n^{uu}(\mathbf{x})$, $\mathbf{Y}_n^{uw}(\mathbf{x})$, $\mathbf{Y}_n^{wu}(\mathbf{x})$, and $\mathbf{Y}_n^{ww}(\mathbf{x})$, to relate the stresses and fluid pressures at location $\mathbf{x}$ in the medium surrounding the fracture to the displacement dislocations $[\mathbf{u}_n]$ and fluid flow $[\mathbf{w}_n]$ on each patch of the fracture. In particular, we substitute the representations of $\mathbf{u}$ and $\mathbf{w}$ into the definitions (4) and (5) of $\mathbf{T}$ and P_f, respectively, to arrive at the linear relationships

$$\delta\mathbf{T}(\mathbf{x},\omega) = \sum_{n=1}^{N} \mathbf{T}_n^u \cdot [\mathbf{u}_n] + \sum_{n=1}^{N} \mathbf{T}_n^w \cdot [\mathbf{w}_n] \tag{26}$$

$$\delta P_f(\mathbf{x},\omega) = \sum_{n=1}^{N} \mathbf{P}_n^u \cdot [\mathbf{u}_n] + \sum_{n=1}^{N} \mathbf{P}_n^w \cdot [\mathbf{w}_n] \tag{27}$$

where we have used $\delta\mathbf{T}(\mathbf{x},\omega)$ and $\delta P_f(\mathbf{x},\omega)$ to signify that these are stress and pressure changes with respect to background fields, due to changes in fracture aperture and flow. We have defined the stress and fluid pressure contributions from each of the N patches of the fracture model as

$$\begin{aligned}
\mathbf{T}_n^u(\mathbf{x},\omega) &= \boldsymbol{\mathcal{A}} : \nabla\mathbf{Y}_n^{uu} + \mathcal{C}\nabla\cdot\mathbf{Y}_n^{wu} && (28)\\
\mathbf{T}_n^w(\mathbf{x},\omega) &= \boldsymbol{\mathcal{A}} : \nabla\mathbf{Y}_n^{uw} + \mathcal{C}\nabla\cdot\mathbf{Y}_n^{ww} && (29)\\
\mathbf{P}_n^u(\mathbf{x},\omega) &= -\boldsymbol{\mathcal{C}} : \nabla\mathbf{Y}_n^{uu} - M\nabla\cdot\mathbf{Y}_n^{wu} && (30)\\
\mathbf{P}_n^w(\mathbf{x},\omega) &= -\boldsymbol{\mathcal{C}} : \nabla\mathbf{Y}_n^{uw} - M\nabla\cdot\mathbf{Y}_n^{ww}. && (31)
\end{aligned}$$

The expressions (26) and (27), giving stress and fluid pressure in terms of the Green's tensors of the medium, provides an explicit relationship between these quantities and the aperture and leak-off from a fluid-driven fracture. For some simple media we can compute analytical or semi-analytical expressions for the Green's functions (Burridge & Vargas, 1979; Norris, 1994; Pride & Haartsen, 1996; Karpfinger et al., 2009). However, the relationship is rather involved for a general heterogeneous poroelastic medium, and difficult to use when it comes to explicit calculations of sensitivities, as needed for solving the inverse problem describe below. Fortunately, we can approximate the integrals of the Green's tensors and compute the sensitivities using a numerical simulator, such as the finite-difference code of Masson et al. (2006); Masson and Pride (2011). In particular, we use the finite-difference approach of Masson et al. (2006) to compute the coefficients (28)-(31) for each of the n patches defining a fracture model. The velocity-stress formulation facilitates relating perturbations in the velocities adjacent to the fracture walls to stress and fluid pressure changes in the surrounding medium. The results of such calculations are shown in Figures 5 and 6 for a linear increase in aperture and a step change in pressure. The temporal variation in the change in the stress component δT_{yy} and the fluid pressure δP_f are plotted in Figure 7 for three locations indicated by open circles in Figures 5 and 6. Note that the change in the fluid pressure exceeds that of T_{yy} at all points and for all times. Thus, the fluid pressure changes appear to dominate the stresses normal to the macroscopic hydro-fracture. This has implications for the evolution of the Coulomb stress around the developing fracture.

2.2.2 Relating Changes in Seismicity to Changes in Stress and Fluid Pressure

In order to relate the fracture displacements to the changes in microseismicity in the surrounding medium, we turn to the rate and state approach of Dieterich (1994) discussed in the Appendix. The use of rate and state estimates of seismicity changes in conjunction with geomechanical and poroelastic simulation is now well established (Passarelli et al., 2013; Hakimhashemi et al., 2014; Segall & Lu, 2015; Zhai & Shirzaei, 2018). Though

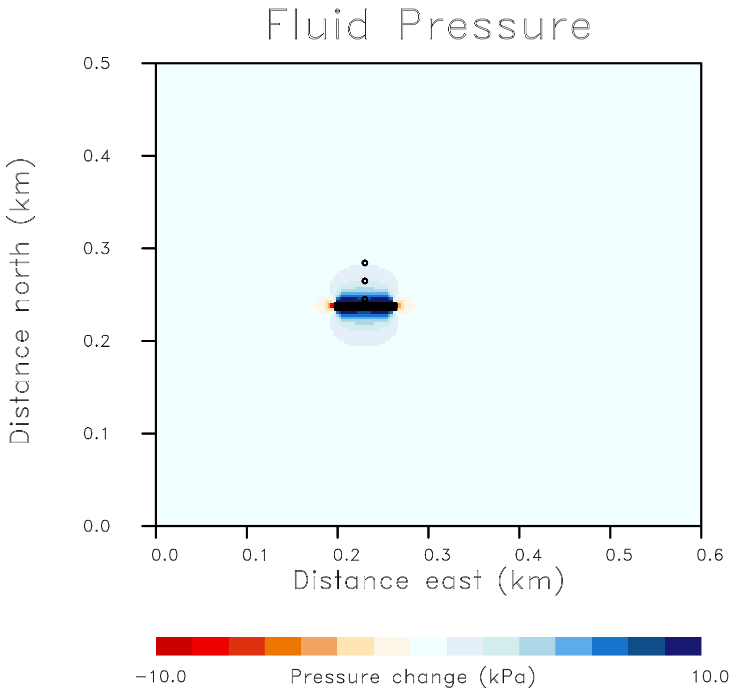

Figure 6. Horizontal cross-section through a fault patch, showing the fluid pressure, P_f, generated by aperture change on a vertical fracture patch and an increase in fluid pressure in the fracture itself. The fracture walls are moving away from each other, increasing the fluid pressure in the region surrounding the fracture. The three open circles to the north of the fracture indicate locations where time series for δT_{yy} and the fluid pressure were extracted. The time series are plotted in Figure 7.

there are other friction laws that can provide a basis for fault rupture (Daub & Carlson, 2008), and hence seismic rate changes, rate- and state-dependent friction has been used successfully in many applications and agrees with the results of careful experiments (Dieterich & Kilgore, 1994; Berthoud et al., 1999; Baumberger et al., 1999). For example, the theory has proven useful in the interpretation of stress transfer due to faulting and its impact on the seismicity following rupture on a fault (Harris & Simpson, 1998; Stein, 1999; Kroll et al., 2017). In this sub-section we relate changes in stress and fluid pressure due to the changing fluid-driven fracture to variations in the rate of microseismicity. Note that we are neglecting the changes in the stress field due to the stress drops that are accumulating from the failure on the cracks generating the microseismic events.

Our starting point is equation (A19) from the Appendix, which relates the ratio of the current seismicity rate to the background seismicity rate, denoted by R, to the change in Coulomb stress, S, given by

$$S = \tau_s - \mu \left(\sigma_n + P_f\right) \tag{32}$$

at a given location in the region around the opening fracture. In this expression σ_n is the normal stress on the crack plane while τ_s is the shear stress acting on the fracture surface, μ is the coefficient of friction associated with the crack surface, and P_f is the fluid pressure within the crack. The exact relationship between the change in the rate of microseismicity around the growing hydro-fracture in a time interval Δt, and the change in Coulomb stress, δS, is given by equation (A19)

$$\ln R - \ln R_o - \ln \left(1 - R{t_c}^{-1}\Delta t\right) = a\delta S, \tag{33}$$

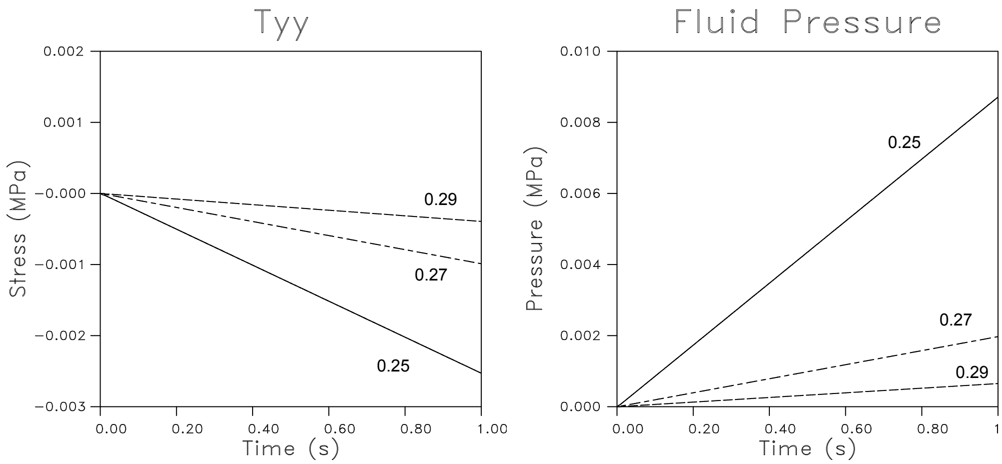

Figure 7. (Left panel) Stress components δT_{yy} for the three observation points indicated in Figure 8. The labels on each curve refer to the y (north-south) location of the observation point for each time series. (Right panel) Fluid pressure changes as a function of time for the three observation points plotted in Figure 7.

where R_o is the ratio in the previous time interval and t_c is the characteristic delay time defined in the Appendix, following equation (A4). The coefficient $a = 1/A\hat{\sigma}_n$ is determined by the background normal stress $\hat{\sigma}_n$ is the region around the fracture and a dimensionless fracture constitutive parameter A that typically lies in the range 0.005-0.015 cited by Dieterich (1994).

Due to the aperture and fluid flow associated with the growing hydro-fracture, the background stress field $\mathbf{T}^o$ is perturbed to a new state

$$\mathbf{T} = \mathbf{T}^o + \delta\mathbf{T}. \tag{34}$$

The stress changes will impact the stability of existing natural or in situ cracks in the vicinity of the fluid-driven fracture. To reduce the possibility confusion, we will use the word crack for the natural or in situ fractures that surround the larger macroscopic fracture. Consider the change in the Coulomb stress on the in situ crack, δS, due to the change in the shear stress ($\delta\tau_s$), the change in normal stress ($\delta\sigma_n$), and the change in pressure in the fluid within it, (δP_f),

$$\delta S = \delta\tau_s - \mu\left(\delta\sigma_n + \delta P_f\right). \tag{35}$$

The change in the Coulomb stress associated with the aperture changes on the rectangular fracture patch described earlier are displayed in Figure 8 for a horizontal and a vertical cross-section through the patch. Note the complexity of the vertical variation in Coulomb stress due to the substantial changes in reservoir permeability and seismic velocity with depth, plotted in Figures 3 and 4 respectively.

The components of the traction vector acting on the plane of the crack, $\mathbf{t}$ are given by

$$t_i = T_{ij} n_j \tag{36}$$

where $\mathbf{n}$ is the normal to the crack plane. The normal component of the traction vector is given by the projection onto $\mathbf{n}$

$$\sigma_n = \mathbf{t}\cdot\mathbf{n} = T_{ij} n_i n_j. \tag{37}$$

The component of shear along the fracture surface, τ_s follows from the decomposition

$$|\mathbf{t}|^2 = \tau_s^2 + \sigma_n^2,$$

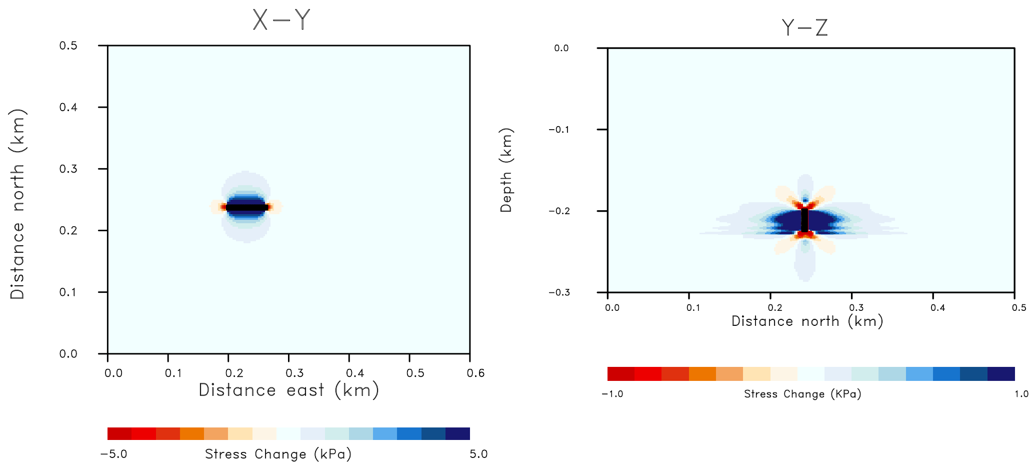

Figure 8. (Left panel) Horizontal cross-section through the Coulomb stress distribution due to aperture change on a vertical fault patch. The Coulomb stresses are estimated for optimally oriented faults. (Right panel) North-south vertical cross-section through the fracture patch at the x (eastern) coordinate of 0.25 km.

thus

$$\tau_s = \sqrt{\mathbf{t} \cdot \mathbf{t} - \sigma_n^2}. \tag{38}$$

Using equations (36) and (37) we can write τ_s in terms of the components of the stress tensor and the normal vector

$$\tau_s = \sqrt{T_{ij} n_j T_{ik} n_k - \left(T_{ij} n_i n_j\right)^2}. \tag{39}$$

Now consider how the stress perturbation (34) changes both the normal and shear stress on the crack and the Coulomb stress. The change in the normal stress is straight-forward to calculate, due to the linear relationship (37) between the normal stress and the stress tensor components,

$$\sigma_n = \left(T_{ij}^o + \delta T_{ij}\right) n_i n_j \tag{40}$$

and

$$\delta\sigma_n = \sigma_n - \sigma_n^o = n_i n_j \delta T_{ij}. \tag{41}$$

Obtaining an expression for the shear stress on the crack surface is more complicated and we must linearize the equation by neglecting terms of second order and higher in the perturbations. Substituting the perturbed stresses into equation (39), which we square for the next few steps of the derivation, produces the expression

$$\tau_s^2 = \left(T_{ij}^o + \delta T_{ij}\right)\left(T_{ik}^o + \delta T_{ik}\right) n_j n_k - \left[\left(T_{ij}^o + \delta T_{ij}\right) n_i n_j\right]^2. \tag{42}$$

Expanding the products and neglecting terms that are greater than first order in the stress perturbation gives

$$\tau_s^2 = T_{ij}^o T_{ik}^o n_j n_k - \left(T_{ij}^o n_i n_j\right)^2 + 2\left(T_{im}^o - T_{lm}^o n_l n_i\right) n_m n_j \delta T_{ij}. \tag{43}$$

We may write the first two terms on the right-hand-side as expressions involving the traction vector and the normal stress due to the background stress field, or more succinctly, in terms of the background shear stress on the crack, τ_s^o,

$$\tau_s = \sqrt{\left(\tau_s^o\right)^2 + 2\left(T_{im}^o - T_{lm}^o n_l n_i\right) n_m n_j \delta T_{ij}}, \tag{44}$$

or as

$$\tau_s = \tau_s^o \sqrt{1 + 2\alpha_{ij} \frac{\delta T_{ij}}{\tau_s^o}}, \tag{45}$$

where, for brevity, we have defined

$$\alpha_{ij} = \frac{\left(T_{im}^o - T_{lm}^o n_l n_i\right) n_m n_j}{\tau_s^o}. \tag{46}$$

Because the term $\delta T_{ij}/\tau_s^o$ varies as the ratio of the stress perturbation to the background shear stress, it is typically very small. Hence, we may approximate (45) using a series expansion, retaining only terms of first order in the ratio of the stress perturbations to the background shear stress,

$$\tau_s = \tau_s^o + \alpha_{ij}\delta T_{ij}, \tag{47}$$

giving a perturbation in shear stress

$$\delta\tau_s = \alpha_{ij}\delta T_{ij}. \tag{48}$$

Putting it all together, we can use equations (40) and (47) to write the perturbation in Coulomb stress as

$$\delta S = \left(\alpha_{ij} - \mu n_i n_j\right) \delta T_{ij} - \mu \delta P_f. \tag{49}$$

Substituting this equation into equation (33) results in an expression relating R to the changes in the stress field and the formation fluid pressure

$$\ln R - \ln R_o - \ln\left(1 - R {t_c}^{-1} \Delta t\right) = c_{ij}\delta T_{ij} - c_f \delta P_f. \tag{50}$$

where

$$c_{ij} = a\left(\alpha_{ij} - \mu n_i n_j\right), \tag{51}$$

and

$$c_f = a\mu. \tag{52}$$

Equation (50), along with equations (26) and (27), form the basis for an inversion of the changes in the seismicity rate to aperture changes in an evolving fluid-driven fracture.

Equation (50) is directly applicable in situations when there is a known set of natural cracks with a consistent orientation $\mathbf{n}$. It can also be applied to statistical distributions with a finite set of natural fracture systems via a weighted sum over the cracks or fractures in each grid block in the medium surrounding the macroscopic hydro-fracture. Lastly, one can apply the approach to a medium with a random distribution of fractures by considering those fractures that are in an optimal orientation for failure in each grid block. For example, in a coordinate system oriented along the principle stress directions, the cracks with optimal orientations for failure have normals in the plane determined by the minimum and maximum principle stresses, T_1 and T_3, respectively. In this coordinate system, a crack with a normal in the T_1–T_3 plane has a Coulomb stress given by

$$S = (T_3 - T_1)\sin\theta\cos\theta - \mu\left(T_1\cos^2\theta + T_3\sin^2\theta - P_f\right) \tag{53}$$

where θ is the angle between the normal and minimum stress axis. By differentiating this equation with respect to θ and setting the resulting expression to zero produces an expression that may be used to determine the orientation of cracks that are most likely to fail. The Coulomb stress is a maximum for a plane rotated by the θ from the minimum stress axis, where θ satisfies

$$\tan(2\theta) = \frac{T_3 - T_1}{\mu\left(T_1 + T_3\right)}.$$

The normal vector of these cracks is then substituted into equations (46) and (51). In the next section we illustrate how one can use the approach, along with observed microseismic activity, to estimate the time-varying changes in aperture associated with a developing fracture.

3 Applications: Imaging the Growth of a Fracture

The locations of microseismic events are useful for determining the overall geometric properties of a hydraulic fracture. For example, micro-earthquakes often define a best fitting planar representation of the fracture, providing its strike, dip, and general dimensions. However, the evolving microseismicity has not been used to image the detailed growth of a fracture as a function of time. In this section we utilize the approach developed in the Methodology section to estimate the opening, or aperture change, of a fluid-driven fracture in both space and time. First the poroelastic code of Masson and Pride (2010) is used to generate displacements, stresses, and fluid pressure changes due to the aperture changes on a specified fracture model. The stresses and fluid pressure changes result in Coulomb stress changes and the generation of seismic events. We use the micro-earthquake rate changes as input to an inversion algorithm for aperture changes, applying the methodology described earlier. Next, we consider the field data set from west Texas presented earlier in the Introduction and Methodology sections, and invert it for time-varying aperture changes associated with a growing hydro-fracture.

3.1 A Synthetic Test

Before considering actual field observations we apply the technique to a set of synthetic seismic events, generated using the poroelastic code of Masson et al. (2006) and Masson and Pride (2010), rate- and state-dependent friction, and a Poisson' probability model. The test case is based upon the hydro-fracture experiment described above. We consider a single 10 minute increment during which aperture changes are imposed upon two developing fractures, as indicated in the upper panel of Figure 9. The finite-

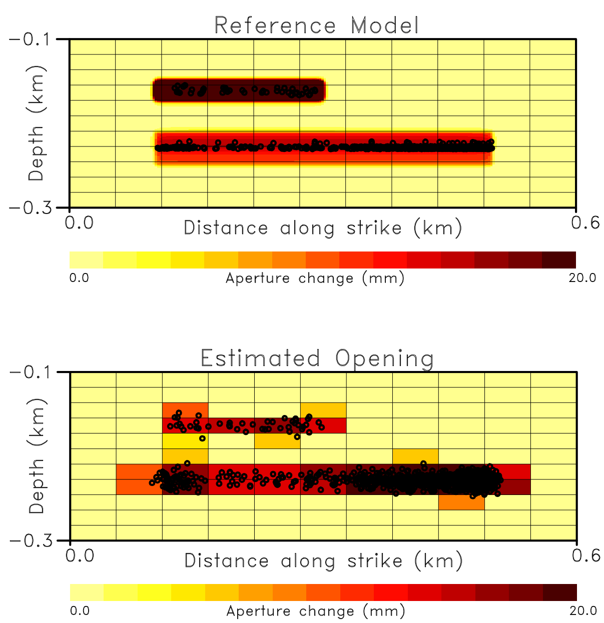

Figure 9. (Top panel) Synthetic aperture changes generated during 10 minutes of fracture growth are indicated by the color scale. The seismicity generated by the Coulomb stress changes are plotted as open circles in this panel. (Bottom panel) Distribution of aperture changes over the fracture, obtained by an inversion of the change in seismicity rates.

difference code of Masson and Pride (2010) is used to compute the velocities, stresses, and pressure changes due to the aperture changes on the fracture. From these quantities we can derive the change in the Coulomb stress using equation (49). Then equation

(A17), which gives the change in the rate of seismic events due to a step change in the Coulomb stress,

$$R(t) = \frac{R_o}{e^{a(S_o - S_1)} + R_o {t_c}^{-1} \Delta t}, \tag{54}$$

can be used to calculate the number of events to be expected in a time interval of length Δt. The determination of the initial rate R_o is best accomplished by establishing a pre-injection background rate through the operation of the seismic array prior to the start of the hydro-fracturing operation. However, because of the added expense of operating a seismic array, this additional baseline data set is often not available and some other technique must be invoked to estimate R_o. One option is to take advantage of a regional network that captures larger magnitude earthquakes and to extrapolate down to events of the size of the micro-earthquakes generated by the opening of the fracture using a universal scaling law (Christensen et al., 2002) or statistical considerations (Kagan & Jackson, 2016).

The generation of micro-earthquakes is assumed to be behave as a Poisson process characterized by the parameter $\lambda = R\Delta t$. That is, the probability of n events in the time interval Δt is assumed to be given by

$$P(n) = \frac{\lambda^n}{n!} e^{-\lambda} \tag{55}$$

(Bickel & Docksum, 2015). The time interval between events for a Poisson process follows an exponential distribution and this can be used to generate a series of events in the time interval Δt for a given cell in the finite-difference grid. The seismicity for each grid cell is computed using a uniform random number generator to estimate the local coordinates within the grid block for each of the n events. A cutoff is used to simulate the finite detection threshold of the seismic network. The seismicity is plotted in the upper panel of Figure 9. Due to the variability of the Coulomb stress distribution in depth, indicated in Figure 8, the seismic events are not evenly distributed in depth. Furthermore, there are areas of fracture aperture change which do not generate any seismic events. This is particularly true for the lower zone, where the events tend to cluster near the center of the fracture. In order to simulate mislocations we added random deviations to each event coordinate, the deviates were drawn from a zero-mean Gaussian distribution with a standard deviation of 6 meters, the estimated location error of the actual events. The final locations used in the test inversion are shown in the lower panel in Figure 9.

In order to relate the temporal and spatial changes in microseismicity directly to the displacements $[\mathbf{u}]$ and fluid leak-off $[\mathbf{w}]$ associated with an evolving hydro-fracture, we make use to the modeling techniques described above. In doing so, we shall take advantage of the characteristics of the actual field site to simplify the inverse problem, both for this synthetic test and for the application below. First, the permeabilities of the shale formations comprising the host rock at the west Texas site are very low, in the range of 1 to 35 micro-Darcies, as indicated by the well log in Figure 3. The values within the interval containing the fracture, above 250 m, are generally 10 micro-Darcies or lower. In contrast, the permeability within the fracture that has opened is much greater, typically more then 1000 times higher. We shall assume that the fluid pressure equalizes quite rapidly within patches of the fracture that are opening, much faster than the fluid equilibrates in the medium surrounding the fracture. Rather then solve for the fluid flow or leak-off from each patch of the fracture, $[\mathbf{w}]$, we shall include a correction for the fluid flow into the formation. In particular, the well pressure recorded during the hydro-fracture is used to estimate the fluid pressure for each fracture patch in the given time interval. That pressure is included as a source term in the poroelastic finite-difference modeling code in order to compute a correction for the leak-off. Second, because the hydro-fracture is perpendicular to the direction of minimum stress for the region, and there is no evidence of significant shearing over the fracture surface, we will assume that the displacement discontinuity is entirely due to aperture change and there is no displacement component parallel to the fracture surface. The displacement discontinuity is then given by

$[u]\mathbf{n}_h$, where $[u]$ is the aperture change and $\mathbf{n}_h$ is the normal to the plane of the hydro-fracture. Combining equations (26) and (50) results in the expression for datum d,

$$d = \ln R - \ln R_o - \ln\left(1 - R{t_c}^{-1}\Delta t\right) - C_p = \sum_{n=1}^{N} \mathcal{L}_n[u_n] \tag{56}$$

which is calculated from the rate changes for a volume of medium adjacent to a given patch of fracture, such as those plotted in Figure 2. In this equation C_p is the correction term for the pressure leak-off, and the linear operator $\mathcal{L}_n$ is obtained from the coefficients in equation (50) projected onto the normal of the hydro-fracture

$$\mathcal{L}_n = c_{ij}\left(\delta\mathbf{T}_n^u\right)_{ij} \cdot \mathbf{n}_h + c_f \delta\mathbf{P}_n^u \cdot \mathbf{n}_h, \tag{57}$$

a relationship between the fracture aperture changes and the changes in the rates of microseismic events at points in the region around the fracture.

Using a minimization algorithm we solve equation (56) in a least squares sense, determining the aperture changes $[u_n]$ that produce matches to the observed changes in the rates of microseismicity. To stabilize the inverse problem we also included regularization or penalty terms. Because the aperture changes are generated by fluid pressure changes due to flow from the injector, we included a term that penalizes large openings that are farther from the trace of the injection well. That is, we can define a penalty function that is based upon the distance to the closest point of the injection well trace. Our solution to the inverse problem is then given by the minimization of the quadratic function of the vector of aperture changes $[\mathbf{u}]$ for the time interval of interest:

$$\mathcal{P}\left([\mathbf{u}]\right) = \sum_{i=1}^{N}\left(d_i - \boldsymbol{\mathcal{L}}_i[\mathbf{u}]\right)^2 + [\mathbf{u}]^t \boldsymbol{\mathcal{D}}_i[\mathbf{u}] \tag{58}$$

where d_i is left-hand-side of equation (56) associated with the rate change in the region adjacent to the i-th pixel, $\boldsymbol{\mathcal{L}}_i$ is the matrix corresponding to the i-th data value, and $\boldsymbol{\mathcal{D}}_i$ is the distance of the i-th pixel to the well trace. The necessary equations for a minimum of the quadratic form are given by $\nabla\mathcal{P}\left([\mathbf{u}]\right) = 0$ where the gradient is taken with respect to the components of the vector $[\mathbf{u}]$. The linear equations are solved for $[\mathbf{u}]$ using an iterative algorithm developed by Paige and Saunders (1982). The estimated aperture changes for the 11 by 11 fracture grid are plotted in the lower panel of Figure 9. The two zones of aperture change are roughly recovered in the solution of the inverse problem. Because of the larger fracture patches and the errors in the event locations, the model tends to extend beyond the ends of the two zones. The errors in the event locations manifest themselves as variations in aperture change amplitudes over the fracture zones and extraneous pixels with aperture change outside of the fracture surface.

The highly localized nature of the Coulomb stresses, evident in Figure 8, suggest that one may be able to ignore the off-diagonal terms in the sensitivity matrix $\mathcal{L}_n$. If the penalty terms were also neglected, then the inversion is equivalent to a direct mapping of the seismicity rate changes into fracture aperture changes. As a test, we constructed this mapping and found that the results were very similar to those shown in Figure 9. Thus, in many cases, it may be possible to formulate the estimation of aperture changes as a direct mapping of the seismicity rate changes.

3.2 The Development of a Hydro-Fracture in West Texas

3.2.1 General Setting

The fracture that we shall study was the first of 8 stages in a west Texas oil field stimulation. The event was isolated in time and was not accompanied by any of the other stages. Furthermore, there was a single stimulated interval within the well, leading to

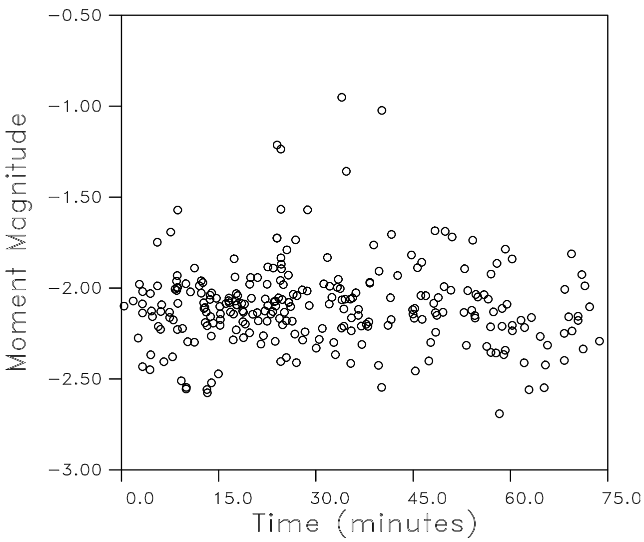

Figure 10. Moment magnitudes of the 280 events as a function of time since the initiation of seismicity.

the growth of a single fracture. As noted by Vasco, Nakagawa, et al. (2019), the associated microseismic events were monitored by a network of 80 Oyo three-component seismometers in four vertical wells surrounding the fracture treatment well (Figure 1). The orientation of each seismometer was determined using calibration shots in the surrounding wells. The compressional and shear wave velocity variations for a vertically-varying model were determined from sonic logs that were run in the central treatment well. The compressional velocity for the interval of interest is plotted in Figure 4, depth averaged over 10 m layers. There are significant large-scale variations of over 30% in the P-velocity. The incoming seismic data stream was scanned with an event detection algorithm in order to associate identified arrivals with a potential microseismic event. A technique known as the Coalescent microseismic mapping (CMM) algorithm, based upon the worked described in Drew et al. (2013), provided event locations without manually determining compressional and shear arrival times. The automated travel time picks were visually reviewed and checked for quality control. The epicentral locations of the microseismic events are plotted in Figure 1 along with the locations of the four wells containing seismometers. We rotated the coordinate system so that the horizontal axis of the fracture plane is oriented along the x-axis and hence the minimum stress direction is along the y-axis. The locations of the events in the plane of the fracture are shown in Figure 2. In Figure 4 the events are displayed on top of a vertical slice through the compressional velocity model. The events are all of small magnitude (Figure 10), generally with magnitudes of around -2.0, and can be classified as microseismicity. With the exception of 5 events at around 20-40 minutes, the magnitude distribution lies between -1.5 and -3.0, and does not change significantly as a function of time. In order to estimate the background seismicity rate, and hence R_o, we consider the historic seismicity in the west Texas region (Frohlich et al., 2016) where natural or tectonic fractures of magnitude 3 or larger occur at a rate of 2 events/year or less. If we extrapolate the rate down to the magnitudes shown in Figure 10, and consider an area the size of our field site (Figure 1), we arrive at a background rate and an estimate for R_o that is equivalent to 1 event of magnitude -2 in the area every 100 minutes.

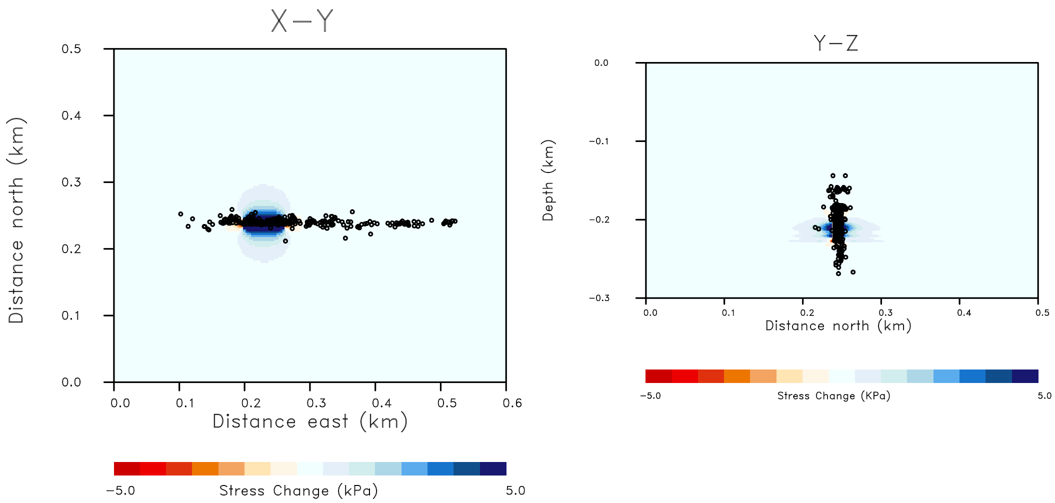

Figure 11. Microseismicity distribution plotted over the Coulomb stress changes due to an aperture change of 1 cm and a fluid pressure increase within the fracture. The Coulomb stress corresponds to the stress required for failure on an optimally oriented fault.

3.2.2 Estimating the Aperture Change

The stress variations in west Texas are quite complicated and tend to rotate across the region (Snee & Zoback, 2016). For the site containing the hydro-fracture the maximum stress direction is the vertical z axis and the minimum stress is in the horizontal direction perpendicular to the fracture plane, the y axis in our local coordinate system. We will refer to the local rotated x direction as local east-west and the y direction as local north-south. In our local coordinate system the principle stresses T_1, T_2, and T_3 are 23.8, 27.3, and 30.0 MPa, respectively. Cracks that are optimally oriented for failure in this stress field have normals that lie in the plane defined by the normal to the macroscopic hydro-fracture and the vertical maximum stress axis. The normals to the cracks most prone to failure are rotated 5.4^o from the minimum stress direction towards the maximum stress direction.

As noted above, we use the poroelastic finite-difference code of Masson et al. (2006) to calculate the sensitivities, $\boldsymbol{\mathcal{L}}_i$, in equation (57). A three-dimensional grid covering a region 600 by 500 by 300 meters in x, y, and z directions, respectively, was used to calculate the stresses, displacements, and pressures due to the aperture changes on the fracture. The grid spacing was 3 meters and uniform along each axis. Zero displacement initial and boundary conditions were imposed on the far field edges of the model. The initial fluid pressure was assumed to be in hydrostatic equilibrium and constant pressure boundaries were specified. Because the displacement components $[\mathbf{u}]$ are associated with aperture changes, we only need the stresses and fluid pressures associated with displacements that are in the direction of the vector $\mathbf{n}_h$, the normal to the fracture plane. The fracture patches, or pixels, are identical to those plotted in Figure 2, dividing the fracture plane into an 11 by 11 grid. The stress changees $\delta T_{xx} = \delta T_{22}$, $\delta T_{yy} = \delta T_{33}$, and $\delta T_{xy} = \delta T_{23}$ are displayed in Figure 5 while the pressure changes in the in-situ pore fluid are shown in Figure 6. Because we are correcting for the fluid leak-off from the fracture and not solving for its value on each patch, there is one unknown aperture change for each fault patch during each time interval. The stress and fluid pressure changes, due to an aperture change of 1 cm over the patch and a pressure of 33 MPa within the fracture, are of the order of 5 kPa to 50 kPa. The fluid pressure was determined from borehole pressure measurements obtained after the initiation of the fracture. Considering wellbore frictional effects and pressure diffusion through the fracture, a pressure of 33 MPa is likely to be larger than the true pressure within the fracture. However, it was found that the calculated displacements and stresses did not change noticeably when the fracture pressure was reduced by a significant amount. The stress and fluid pressure changes around the fracture are much smaller in magnitude than the regional background stresses of around 24-30 MPa. The Coulomb stress change, shown for a horizontal and vertical plane in Figure 11, changes due to the aperture change on the fracture patch, given by the expression (32), indicate that the likelihood of failure is increased around the opening fracture primarily due to the increase in pore fluid pressure. The zone of Coulomb stress change is confined to the area of the fracture patch and extends some 50 meters outward from the fracture plane. A plot of the projection of microseismic events onto horizontal and vertical planes this figure shows that the extent of the region of increased Coulomb stresses is compatible with the distribution of observed microseismicity.

With the methodology described above, we can use the temporal and spatial distribution of microseismic events to infer the geometry of the evolving fracture. In our analysis we utilize the 11 by 11 grid to define 121 fault patches and we examine microseismicity variations in 10 minute time intervals for each patch, as shown in Figure 2. All events within a given fault patch location were used to compute the number of events in a given time interval, averaging over coordinate direction perpendicular to the given pixel. The number of events in each patch for each time interval were used to compute the rates $R(t)$ for each fault patch. Due to the limited sensitivity of the seismometers there will be a detectability threshold for the seismic monitoring array. Thus, only a fraction, f, of the total number of events will be identified and located. Because the magnitude distribution does not seem to change in time, we shall assume that the detectible fraction f does not change from time interval to time interval. This implies that the ratio of detectible events for two successive time intervals should be identical to the ratio of total events for those two intervals.

As for the synthetic test, we set up the system of equations (56) and the equivalent quadratic misfit functional (58) that comprise the inverse problem. The integrated Green's tensors associated with each of the fault patches are computed using the poroelastic finite difference code (Masson & Pride, 2010). The integration along the y axis extended 50 meters in both directions away from the fault plane. With these Green's tensors we computed the quantities necessary to define the coefficients in equations (56) and (57), relating fracture aperture changes to variations in the rates of microseismic events. For each of the five time intervals over the 50 minutes we have 121 equations in the same number of unknowns. The system of equations is solved in a few minutes of CPU time using the least squares QR (LSQR) algorithm described in Paige and Saunders (1982), an iterative approach suited for linear systems. The method successively adds singular vectors to the solution as necessary to fit the observations

The resulting solutions of the inverse problem for the five time intervals are plotted in Figure 12 as cumulative aperture changes during the first 50 minutes of injection. Over the initial 10 minutes of injection one observes early aperture changes near the well trace and propagating to the west in a shallow formation. There appears to be an upper and lower zone of propagation during this earliest time interval. Between 10 and 20 minutes after the start of injection there are notable aperture changes from 150 to 200 meters to the east of the injection well in the shallow formation and westward propagation of about 100 meters. These trends continue for the next 30 minutes, defining a shallower zone of significant asymmetric fracture propagation to the east and a deeper zone of more limited and more symmetric fracture opening, extending about 50 meters from the injection well. The general properties of the solution shown in Figure 12 agree with numerical coupled modeling of the hydraulic fracturing experiment. In particular, a coupled geomechanical-hydrological model of the experiment indicated peak aperture changes of around 2.5 cm. Furthermore, during the first 16 minutes of the injection both an upper and a lower zone of fracture opening appeared in the simulation, as indicated

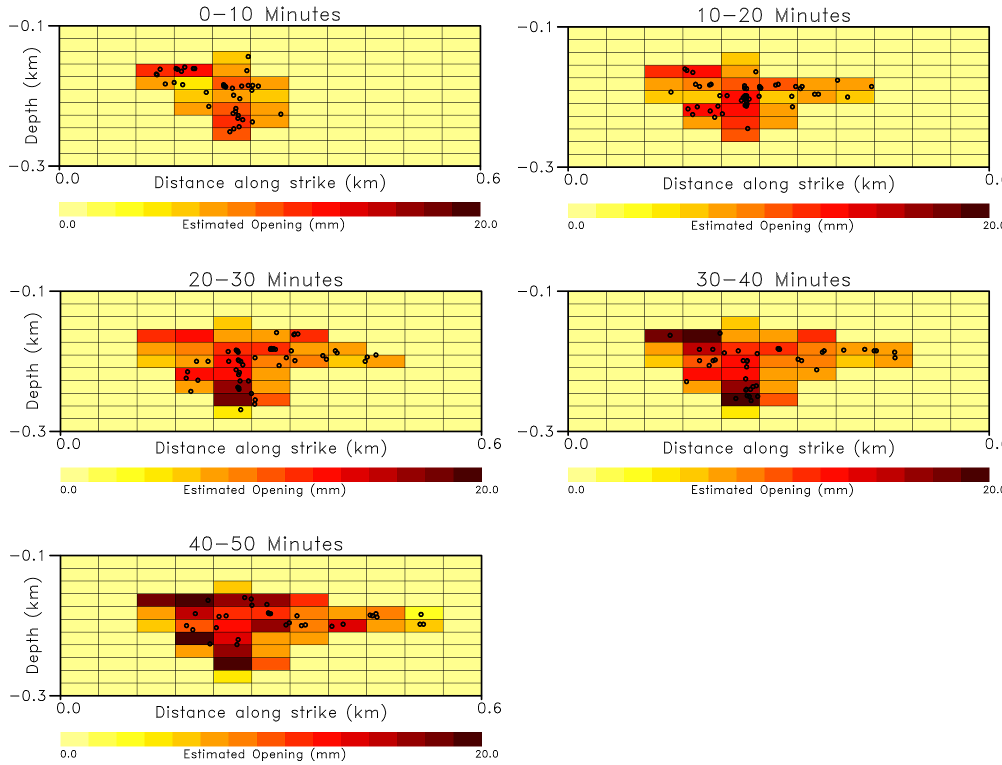

Figure 12. Aperture changes for five 10 minute intervals used to image the fracture propagation. The boundaries of the fault patches are indicated by the thin black lines while the microseismic events during each time interval are indicated by the open circles.

in Figure 12. However, the results of the numerical simulation displayed symmetric behavior about the injection well and did not display preferential propagation to the east. The asymmetric propagation observed in the solutions to the sequence of inverse problems can be induced by stress gradients in the surrounding medium (Dahm et al., 2010).

The micro-earthquakes that are used to calculate the rate changes are subject to mislocation errors that can produce changes in the density of events in a given grid element. This will produce errors in the estimated rates for each time interval, resulting in variations in the estimates of aperture changes. The exact relationship between the earthquake locations and the aperture changes is nonlinear, as indicated by the relationship in equation (56). In order to estimate the uncertainty of the aperture changes due to mislocation errors, we conducted a series of inversions with perturbed earthquake locations. The size of the perturbations in the locations were determined by the estimated errors provided by the location algorithm (Drew et al., 2013), an error ellipse with a diameter of 12.2 m in the horizontal direction and 12.8 m in the vertical direction. The event locations shown in Figure 1 were perturbed in each direction by deviates drawn from a Gaussian distribution with a standard deviation of 6.3 m. A total of 100 inversions were conducted, each with a set of perturbed event locations, and the results were used to compute a sequence of aperture changes for each fault patch. The mean and standard deviation were computed for the aperture changes for the 10 minute time interval from start of injection until the end of pumping and are shown in Figure 13. The largest variations, standard errors of around 4 mm, tend to be located on the edges of the areas with a few located events. In these regions a shift in the event location can move it into another fracture patch, changing the estimated rates by a significant fraction. To

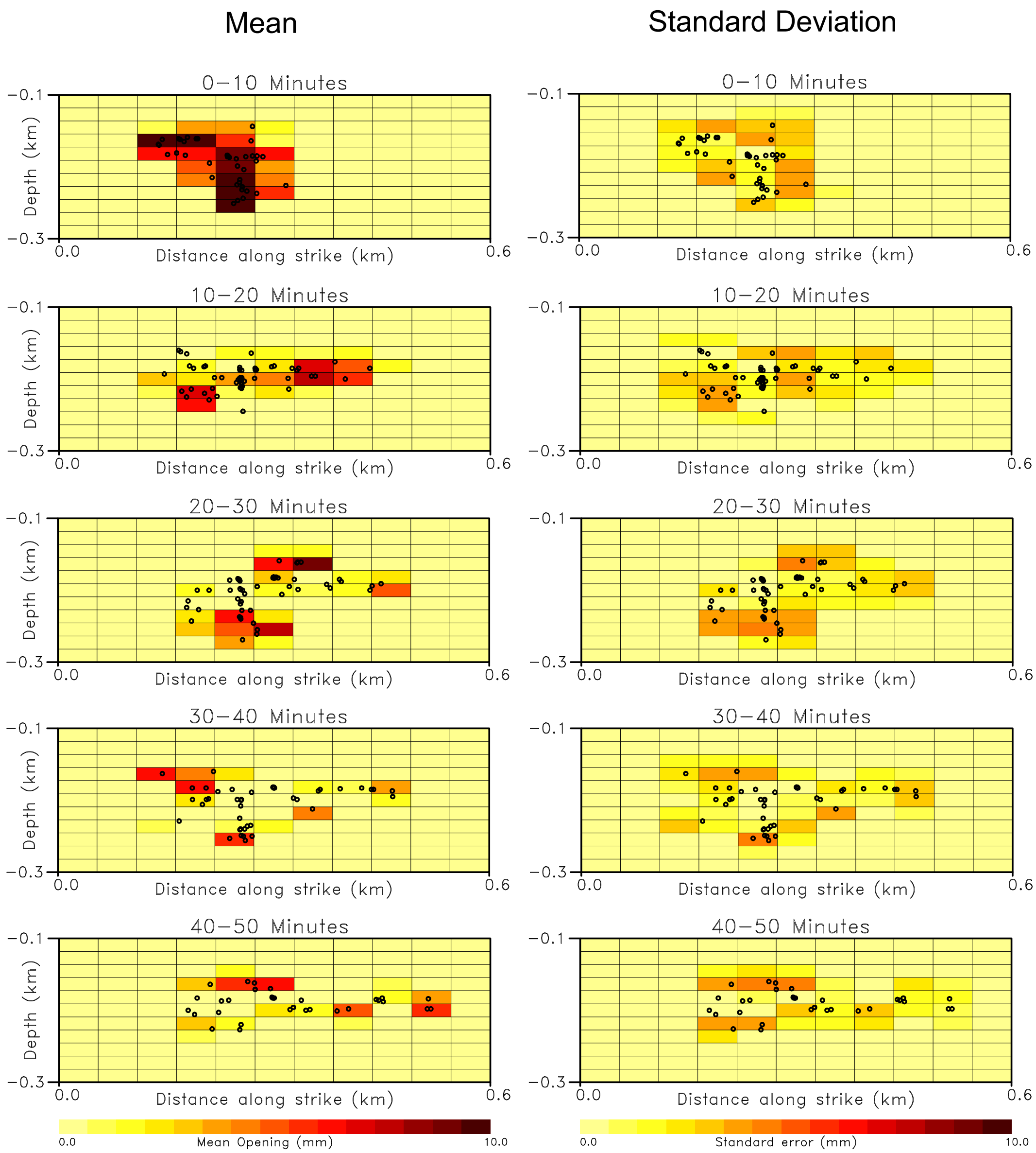

Figure 13. Mean and standard deviation of a distribution of 100 inversion results. Each inversion used earthquake data containing added Gaussian mislocation errors with a standard deviation of 6.3 meters. The aperture changes for each 10 minute increment are shown in the panels. The open circles denote the seismic events observed during each 10 minute interval.

determine the impact of mislocations on the cumulative aperture changes we considered the sum of the changes over each of the increments as a random variable. The total changes

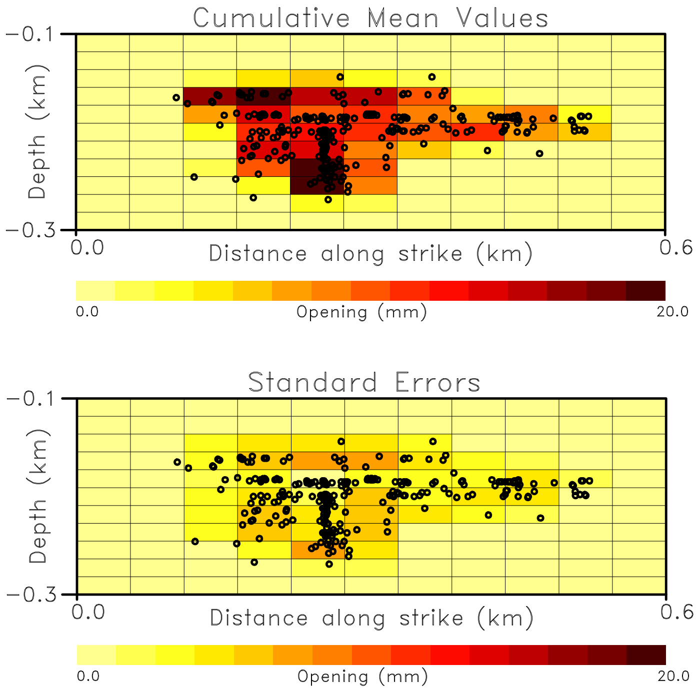

Figure 14. (Upper panel) Mean of 100 inversions of perturbed event locations, presenting the average aperture change for each fracture patch during the first 50 minutes of injection. (Lower panel) Standard error of the cumulative aperture changes over the entire 50 minute interval. The open circles in each panel represent the locations of the complete set of micro-earthquakes used in the analysis.

over the entire 50 minute interval, the means of the 100 realizations, are shown in Figure 14. The resulting cumulative mean aperture changes, obtained by averaging over the 100 realizations, display the general features of our inversion of the unperturbed data, shown in Figure 12. That is, the extent of the region of significant aperture changes are very similar, as are the peak changes of around 20 mm. Both solutions contain upper and lower zones of larger changes and asymmetric growth in the positive strike direction (to the northeast). The standard error of the set of solutions is of the order of 30% of the mean values with a peak value of 7.3 mm. The largest errors are found at the edges of the cloud of events, where changes in event locations are likely to lead to larger rate changes in neighboring fault patches.

In addition to the numerical solution, we can use the observed injection rate (Figure 15) to perform a rough validation of the volume changes of the fracture with time. That is, one can integrate the flow rate to calculate the cumulative injected fluid volume as a function of time as shown in the right panel of Figure 15. Note the fluctuations in rates after 50 minutes of injection. From the aperture changes in Figure 12, and the area of each fracture patch, we can calculate the fracture volume change as a function of time, and the cumulative fracture volume. The time-varying injected volume may be compared with the cumulative fracture volume change, obtained by summing over the aperture changes in each 10 minute time increment (Figure 15). There is generally good agreement between the injected volume and the fracture volume for the first 40 minutes of injection. After 40 minutes the injection volume is systematically larger then the estimated frac-

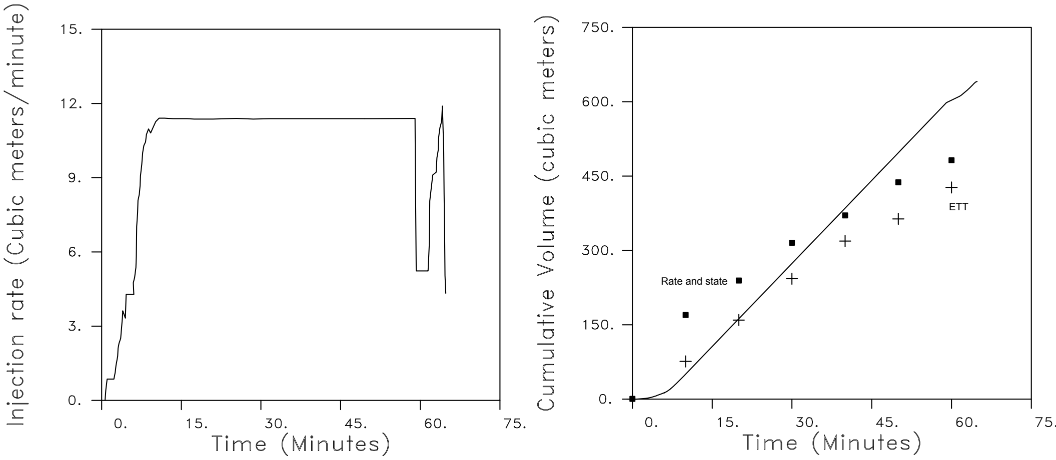

Figure 15. (Left panel) Time-varying injection rate. (Right panel) Comparison between the cumulative injected fluid volume and the estimated cumulative volume change obtained by summing all of the aperture changes for each of the five 10-minute intervals. Estimates are shown for aperture changes based upon a rate- and state-dependent friction model and for change calculated using the extreme threshold theory (ETT) based upon equation (59).

ture volume. This discrepancy may be due to variable fluid leak-off at later times due to increasing permeability around the fracture, particularly near the injection well, leading to fluid flow into the surrounding medium. Alternatively, the injection rate does deviate significantly at the later time intervals (see Figure 15) possibly leading to unreliable values at these later times.

4 Discussion and Conclusions

A rate and state-dependent formulation of failure, coupled with methods from poroelasticity, provides a quantitative relationship between aperture changes on a fluid-driven fracture and changes in seismicity in the region surrounding the fracture. The approach is valid for a fully three-dimensional medium and in the presence of anisotropy. The theory provides expressions for the relative contributions of both shear along the fracture plane and aperture changes, along with fluid leak-off from the fracture itself. The aseismic deformation and fluid flow from the fracture strains the surrounding medium and generates stress and pore pressure changes, leading to observable microseismicity around the macroscopic fracture. Thus, the quasi-static deformation of the fracture is characterized by the seismic events that are generated. As a consequence, the monitoring of microseismicity has become the most common geophysical method for estimating the properties of a macroscopic hydro-fracture (Eaton, 2018). However, it has been pointed out that aseismic strain may account for much of the deformation associated with faults or fractures stimulated by fluid injection (Guglielmi, Elsworth, et al., 2015; Wynants-Morel et al., 2020). This implies that most of the deformation associated with the opening of the fracture will be missed if one simply considers the associated microseismicity. One option is to measure nearby quasi-static deformation directly using instruments in nearby monitoring wells. Currently, such downhole instruments are rarely deployed, but they may become more common with advancements in monitoring technology, such as developments in distributed strain sensing (DSS) (Zhang et al., 2020), distributed acoustic sensing (DAS) cables (Daley et al., 2013), and broadband seismometers. Direct strain monitoring can also mitigate another issue related to aseismic deformation, the lack of seismicity due to sealed and plastically deforming micro-fractures. That is, mineralization can prevent seismic slip on a micro-fracture. In addition, fractures in formations such as shales, have a tendency to deform plastically without exciting significant elastic wave energy. This aseismic deformation may still be detected by downhole strain sensors or broadband instruments.

The results from this study are promising, but there are several potential complicating factors that need to be examined in future studies. First, a critical aspect that needs further exploration is the variation of the coefficient $a = 1/A\hat{\sigma}_n$ in equation (33) between different formations, as the parameter A describes the sensitivity of the rate of events to the changes in Coulomb stress. Thus, differences in A between formations can map directly into differences in estimates of aperture changes within those formations. This suggests that laboratory studies should be undertaken to determine A in the formations present in a particular study area. Alternatively, it may be possible to use observations from the region immediately around the well to calibrate the model for each major formation. Secondly, we assumed that the fracture evolved in relative isolation and did not interact with either a nearby or an intersecting macroscopic fracture. Such interactions can be handled by modifying the conceptual model to include such larger-scale features as they are revealed in the observed seismicity. Thirdly, for the current formulation we have assumed constant properties over the time interval of interest, and have not accounted for changes in poroelastic properties over time. For example, we do not account for the changes in permeability or mechanical properties that are associated with the slip on micro-fractures surrounding the fault. It has been shown that fluid injection into a fractured porous medium produces a host of changes to the mechanical and flow properties (Berryman, 2016; Pride et al., 2016), leading to time-varying coefficients in the governing equations (1) and (2) and the constitutive relationships (3) and (4). It should be possible to account for such changes by treating the surrounding formations as an effective medium (Pozdniakov & Tang, 2004) and using the observed seismicity to estimate changes due to the presence of reactivated fractures. Such changes could be added incrementally, for example during each 10 minute increment in our current study. The evolution of poroelastic properties could also be used to improve estimation of resource recovery. As noted above, it is also possible to incorporate the properties of existing nature fractures. Thus, as indicated in the Methodology section, one could replace the failure criteria for a optimally oriented fault by one for fractures with a specific orientation, or for a set of orientations. One could even replace the deterministic inversion for aperture change with a stochastic estimation scheme, accounting for the statistical properties of the fractures in the formations. Such methods have been used to estimate stress fields from centroid moment tensors (Terakawa & Matsu'ura, 2008). Additional applications are needed in order to further test the approach and to realize it's limitations and ways to overcome them.

It should be noted that there are other approaches that lead to an exponential dependence of the seismicity rate on Coulomb stress, such as the extreme threshold theory (ETT) applied to seismic events by Bourne et al. (2018). The method acknowledges the heterogeneity of fault and fracture properties within the Earth, as well as the heterogeneity of formation characteristics. It is hypothesized that the failure associated with microseismic events represent the extremes of the heterogeneities, found within the tails of these distributions of properties. Furthermore, the structural heterogeneities act to concentrate and localize shear stress and seismicity at a scale that is too small to characterize in a deterministic fashion. Indeed, it has shown that stress concentrations due to random heterogeneities are sufficient to generate the stresses necessary for Coulomb failure at The Geysers, without the need for a critically stressed crust (L. R. Johnson & Majer, 2017). Bourne et al. (2018) invoke Extreme Threshold Theory (Picklands, 1975; Cole, 2001) in order to model the probabilities of such failure, which suggests that generalized Pareto distributions govern the statistics, with the exponential distribution being the simplest example. This statistical formulation produces a relationship of the form,

$$\mathcal{N} = \exp\left(\theta_0 + \theta_1 \delta S\right) \tag{59}$$

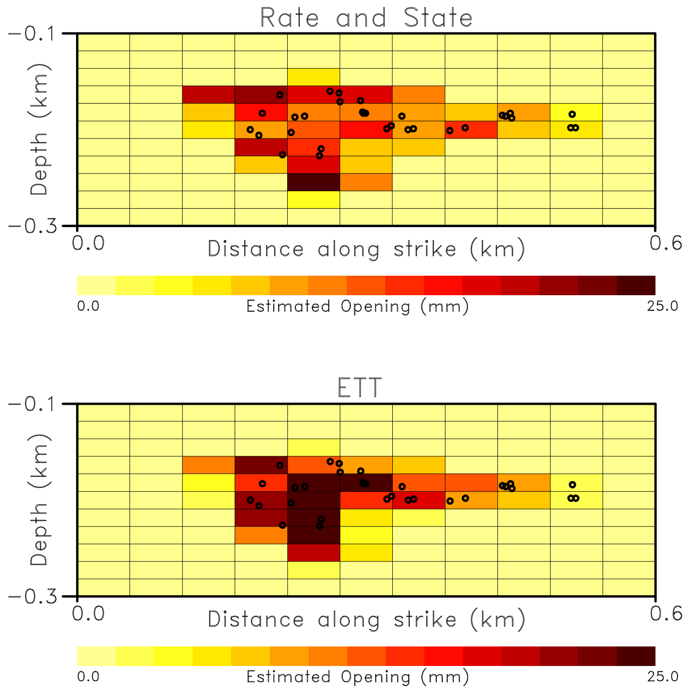

Figure 16. Comparison between aperture changes estimated using the method described in this paper and an approach utilizing the extreme threshold theory of Bourne et al. (2018)

where $\mathcal{N}$ is the cumulative number of earthquakes per unit thickness of formation. The parameter θ_0 scales the relationship and was set equal to 1.0 for this estimation. The parameter θ_1 was adjusted to optimize the fit to the rate data, and had a value of 0.003. We can compare the solution based upon extreme threshold theory to the one based upon rate and state-dependent frictional failure. The overall pattern of aperture changes is similar for the two methods but there are differences in the detailed distribution of aperture changes (Figure 16). Both methods provide fair agreement between the injected fluid volume and the estimated temporal variation of fracture volume for the early injection times, based upon these aperture changes (see Figure 15). Additional work is needed to compare the two theories in other field and laboratory settings.

5 Appendix: Relating Stress Changes to Temporal Variations in Seismicity

1 Formulation for a general variation in Coulomb stress $S(t)$

Our interest is in the changes in seismicity in the volume of rock surrounding an evolving fluid driven fracture. In particular, we shall assume that the fracture has been initiated and the injected fluid and pressure changes lead to aperture changes and shear on the fracture plane. The developing hydro-fracture induces stress changes in the surrounding region that promote movement on favorably oriented, natural, in-situ fractures. We consider the changes in the rate of microseismic events in a rectangular volume of rock adjacent to the hydro-fracture. Therefore, within this volume we will fix our location at a point $\mathbf{x}$ and only consider temporal changes in the quantities of interest at that point. Following this discussion we will allow the location to vary within the region surrounding the hydro-fracture. Our starting point is the rate and state approach of Dieterich (1994) but written in the condensed form presented in Dieterich et al. (2000). We adopt the somewhat abbreviated notation where we consider the ratio $R = r_c/r_b$ of the current rate of microseismic activity, r_c, to the background or historical seismicity rate, r_b, as in Segall and Lu (2015). In Dieterich (1994) and Dieterich et al. (2000) the ratio of current seismic to background microseismicity, R, is expressed in terms of the state variable γ

$$R = \frac{1}{\gamma \dot{\tau}_b} \tag{A1}$$

where $\dot{\tau}_b$ is the background stressing rate and the dot denotes the derivative with respect to time. The state variable γ depends upon the slip history of the deforming surface and evolves according to

$$d\gamma = \frac{1}{A\hat{\sigma}_n}\left[dt - \gamma dS\right] \tag{A2}$$

where A is a dimensionless fault constitutive parameter, typically in the range 0.005-0.015, and S is a modified Coulomb stress function defined as

$$S = \tau_s - \mu\left(\sigma_n + p_f\right). \tag{A3}$$

In this expression for the Coulomb stress S, the quantity τ_s signifies the shear stress on the fault/fracture surface, σ_n denotes the normal stress acting on that surface, p_f is the fluid pore pressure, and μ is the coefficient of friction associated with the fracture plane. The quantity $\hat{\sigma}_n$ is the constant, average background normal stress in the region. Using equation (A1) to solve for γ in terms of R and differentiating with respect to time gives a relationship between their derivatives that we can use to write equation (A2) in terms of R. Specifically, equation (A2) may be re-written as

$$t_c \frac{dR}{dt} = R\left[\dot{C} - R\right], \tag{A4}$$

where, following Segall and Lu (2015), we have defined t_c, the characteristic delay time $t_c = A\hat{\sigma}_n/\dot{\tau}_b$, and $\dot{C}$, the time derivative of the Coulomb stress change normalized by the rate of change of the background stress, $\dot{C}(t) = \dot{S}(t)/\dot{\tau}_b$.

2 Solution of the Riccati equation for $R(t)$

As pointed out by Wenzel (2017), equation (A4) is a reduced form of the general Riccati equation [see for example Ince (1956) and Boyce and Diprima (2012)], an initial value problem for R that depends upon the rate at which the Coulomb stress evolves over time. It has long been known that the Riccati equation may be transformed into a second-order linear homogeneous equation, as shown in Boyce and Diprima (2012). We use this transformation to derive a solution of the particular form of the Riccati equation given by the expression (A4). In particular, the solution of the general Riccati equation,

$$\frac{dR}{dt} = q_0 + q_1 R + q_2 R^2, \tag{A5}$$

where $q_0(t)$, $q_1(t)$, and $q_2(t)$ are general functions of t, can be related to the solution $y(t)$ of a linear, second-order, homogeneous ordinary differential equation

$$q_2 \frac{d^2 y}{dt^2} - [\dot{q}_2 + q_1 q_2] \frac{dy}{dt} + q_2^2 q_0 y = 0, \tag{A6}$$

where the dot denotes the derivative with respect to t. Specifically the solution to the Riccati equation (A5) is related to the solution $y(t)$ to the linear second-order equation (A6) via the relationship

$$R(t) = -\frac{\dot{y}(t)}{y(t) q_2(t)}. \tag{A7}$$

For the particular form of the Riccati equation (A4), we have $q_0(T) = 0$, $q_1(t) = \dot{C}(t)/t_c$, and $q_2(t) = -1/t_c$. Thus, in our case the linear second-order equation is

$$-\frac{1}{t_c}\frac{d^2 y}{dt^2} + \frac{\dot{C}}{t_c^2}\frac{dy}{dt} = 0, \tag{A8}$$

with the solution

$$y(t) = e^{\alpha} \int_0^t e^{C(x)/t_c} dx + \beta \tag{A9}$$

where α and β are integration constants. Therefore, the solution $R(t)$ follows from equation (A7)

$$R(t) = \frac{t_c e^{C(t)/t_c}}{B + \int_0^t e^{C(x)/t_c} dx} \tag{A10}$$

where B is a composite function of the integration constants

$$B = \beta e^{-\alpha}. \tag{A11}$$

Using the fact that at time zero, before the stress change, the ratio R is equal to some value R_o, we can solve for the constant B

$$B = \frac{t_c}{R_o} e^{C(0)/t_c}. \tag{A12}$$

Hence, equation (A10) takes the particular form

$$R(t) = \frac{R_o e^{C(t)/t_c}}{e^{C(0)/t_c} + R_o {t_c}^{-1} \int_0^t e^{C(x)/t_c} dx} \tag{A13}$$

which can be written in terms of the Coulomb stress $S(t)$ because

$$\frac{1}{t_c} C = \frac{1}{t_c \dot{\sigma}_b} S = \frac{1}{A \hat{\sigma}_n} S = aS \tag{A14}$$

where we have defined $a = 1/A\hat{\sigma}_n$. Therefore the complete solution for $R(t)$ for a general temporal variation in Coulomb stress $S(t)$ is given by

$$R(t) = \frac{R_o e^{aS(t)}}{e^{aS(0)} + R_o {t_c}^{-1} \int_0^t e^{aS(x)} dx}. \tag{A15}$$

Note that the solution (A15) can be shown to be equivalent to that presented by Wenzel (2017) for the particular form of the Riccati equation (A4). It is also of the same form as the solution of Heimisson and Segall (2018), obtained using a different derivation based upon the time to instability for a population of sources. We can verify that (A13) solves equation (A4) by simple substitution. An alternative form of the solution is obtained by multiplying the numerator and denominator by $e^{-S(t)}$

$$R(t) = \frac{R_o}{e^{aS(0)} e^{-aS(t)} + R_o {t_c}^{-1} e^{-aS(t)} \int_0^t e^{aS(x)} dx}, \tag{A16}$$

a form that is somewhat similar to the solution given Wenzel (2017) and to that of Dieterich (1994). Examples of the numerical evaluation of (A15) for a step and logarithmic change are shown in Figure 17. As illustrations of this form for $R(t)$, we consider explicit expressions for a step and a linear increase in Coulomb stress.

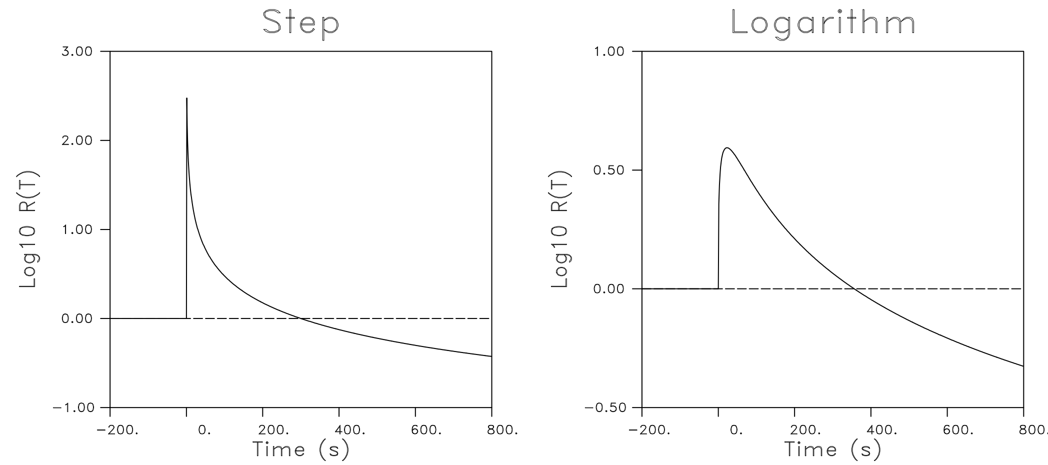

Figure 17. Rate change due to a step change (left) and a logarithmic variation (right) in the Coulomb stress.

3 A step change in the Coulomb stress

Consider a step change in Coulomb stress at a location in the region around the opening macroscopic fracture. That is, the Coulomb stress jumps from an initial or background value of S_o at $t = 0$, to a new value S_1 for $t > 0$. Thus, the integrand is constant in (A16) and we may write the equation as

$$R(t) = \frac{R_o}{e^{a(S_o - S_1)} + R_o {t_c}^{-1} \Delta t}, \tag{A17}$$

which decays as the time interval Δt grows in length. This temporal decay, following the initial jump in the rate of seismic events, is evident in Figure A1. If the characteristic time is long in comparison to the time interval, $t_c >> \Delta t$, we have

$$R(t) = R_o e^{a(S_1 - S_o)}, \tag{A18}$$

signifying the amplification of the seismicity rate from the previous or background value R_o for the given jump, $\delta S = S_1 - S_o$, in Coulomb stress. We can use equation (A17) to relate the change in Coulomb stress to the ratio of the rates of seismic events before and after the jump in stress that occurred during the time interval Δt

$$a\delta S = \ln R - \ln R_o - \ln\left(1 - R{t_c}^{-1}\Delta t\right). \tag{A19}$$

This relationship is useful for estimating the aperture change that corresponds to the change in the rate of seismicity.

4 A linear variation in the Coulomb stress: $S(t) = S_o + \dot{S}_o t$

A linear temporal variation is particularly useful when modeling Coulomb stress changes due to fluid added to a fracture at a constant rate. Furthermore, one can decompose a general stressing history into a sequence of linear segments. For a linear increase in Coulomb stress as a function of time we can explicitly evaluate the integral in expression (A13) and derive an analytic expression for $R(t)$. That is for a Coulomb stress $S(t)$ that varies as

$$S(t) = S_o + \dot{S}_o t, \tag{A20}$$

where S_o is the background Coulomb stress and $\dot{S}_o$ is the rate of Coulomb stress change associated with the variation in the volume of the fluid-driven fracture for a give time

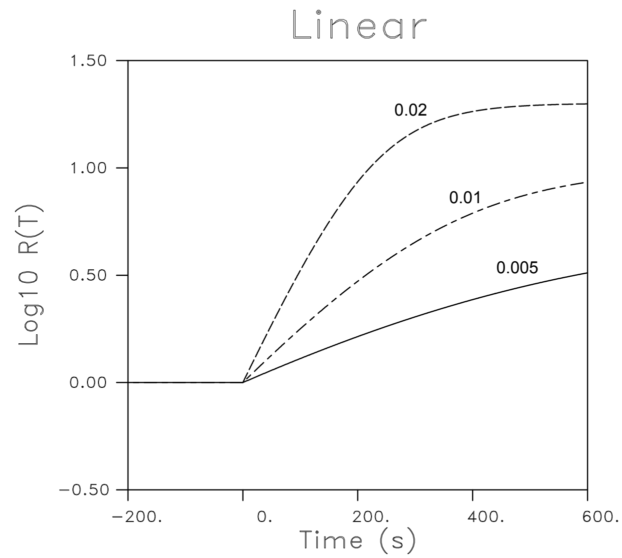

Figure 18. Rate change corresponding to a linear variation in Coulomb stress. The numerical labels indicate the value of ϵ associated with each curve.

interval, we can write equation (A15) as

$$R(t) = \frac{e^{aS(t)}}{(1-\epsilon)\, e^{aS(0)} + \epsilon e^{aS(t)}} \tag{A21}$$

where ϵ is the ratio of the background stressing to the rate of change of the Coulomb stress due to the change induced by the evolving fracture, $\epsilon = \dot{\sigma}_b/\dot{S}_o$, typically ϵ is a very small quantity. Equation (A20) can be shown to be equivalent to the form given by Dieterich (1994) if we multiply both the numerator and the denominator by $e^{-aS(t)}$. In Figure 18 we plot three examples of the temporal variation of $R(t)$ for different values of ε. As ε decreases the curves of $\log R(t)$ approach a straight line, as indicated in equation (A21).

In the vast majority of situations the changes in Coulomb stress due to the fluid volume added to the fracture will be much greater than the background stressing rate and we will have $\epsilon = \dot{\sigma}_b/\dot{S}_o \ll 1$, and we can neglect the ϵ in the parenthesis in equation (A21). Inverting equation (A18) and taking the logarithm, we can produce a direct relationship between the change in Coulomb stress, $\delta S = S(t) - S_o = \dot{S}_o \Delta t$, where Δt is the time interval under consideration, and a change in the rate of associated seismic events $R(t)$:

$$a\delta S = -\ln\left(R^{-1} - \epsilon\right) = \ln R - \ln\left(1 - \epsilon R\right). \tag{A22}$$

Because ϵ depends upon $\dot{S}_o$, equation (A22) is an implicit equation for the rate of Coulomb stress change over a given time interval, unless ϵ is small enough to be neglected.

Acknowledgments

The development of the technique for the calculation of fracture aperture changes from observed seismicity was supported by the U.S. Department of Energy, Office of Science, Office of Basic Energy Sciences, Chemical Sciences, Geosciences, and Biosciences Division under contract number DE-AC02-05- CH11231. The analysis of the microseismicity associated with the aperture changes on the opening hydro-fracture was supported by Chevron. The data shown in Figures 2 and 10 are available for download from the Zenodo archive under the title Microseismicity for hydro-fracture experiment, with the digital identifier doi/10.5281/zenodo.3736809.

References

Ajo-Franklin, J., Daley, T., Butler-Veytia, B., Peterson, J., Wu, Y., Kelly, B., & Hubbard, S. (2012). *Multi-level continuous active source seismic monitoring (ml-cassm): Mapping shallow hydrofracture evolution at a tce contaminated site.* Society of Exploration Geophysics Annual Meeting.

Aki, K., & Richards, P. G. (1980). *Quantitative seismology.* San Francisco: Freeman and Sons.

Albright, J. N., & Pearson, C. F. (1982). Acoustic emissions as a tool for hydraulic fracture locations: Experience at the fenton hill hot dry rock site. *Society of Petroleum Engineers Journal*, *22*, 523-530.

Baumberger, T., Berthoud, P., & Caroli, C. (1999). Physical analysis of the state- and rate-dependent friction law. ii. dynamic static friction. *Physical Review B*, *60*, 3928-3939.

Berryman, J. G. (2016). Role of fluid injection in the evolution of fractured reservoirs. *International Journal of Engineering Science*, *103*, 45-58.

Berthoud, P., Baumberger, T., G'Sell, C., & Hiver, J.-M. (1999). Physical analysis of the state- and rate-dependent friction law: Static friction. *Physical Review B*, *59*, 14313-14327.

Bickel, P. J., & Docksum, K. A. (2015). *Mathematical statistics: Basic ideas and selected topics.* Boca Raton: CRC Press.

Biot, M. A. (1941). General theory of three-dimensional consolidation. *Journal of Applied Physics*, *12*, 155-164.

Biot, M. A. (1962). Mechanics of deformation and acoustic propagation in porous media. *Journal of Applied Physics*, *33*, 1482-1498.

Bourne, S. J., Oates, S. J., & van Elk, J. (2018). The exponential rise of induced seismicity with increasing stress levels in the groningen gas field and its implications for controlling seismic rish. *Geophysical Journal International*, *213*, 1693-1700.

Boyce, W. E., & Diprima, R. C. (2012). *Elementary differential equations and boundary value problems.* New York: John Wiley and Sons.

Bunger, A. P., & Detournay, E. (2008). Experimental validation of tip asymptotics for a fluid-driven crack. *Journal of Mechanics and Physics of Solids*, *56*, 3101-3115.

Burridge, R., & Knopoff, L. (1964). Body force equivalents for seismic dislocations. *Bulletin of the Seismological Society of America*, *54*, 1875-1888.

Burridge, R., & Vargas, C. A. (1979). The fundamental solution in dynamic poroelasticity. *Geophysical Journal of the Royal Astronomical Society*, *58*, 61-90.

Christensen, K., Danon, L., & Bak, P. (2002). Unified scaling law for earthquakes. *Proceedings of the National Academy of Sciences*, *99*, 2509-2513.

Cole, S. (2001). *An introduction to statistical modeling of extreme values.* London: Springer Verlag.

Dahm, T., Hainzl, S., & Fischer, T. (2010). Bidirectional and unidirectional fracture growth during hydrofracturing: Role of driving stress gradients. *Journal of Geophysical Research*, *115*, 1-18.

Daley, T. M., Freifeld, B. M., Ajo-Franklin, J. B., Shan, D., Pevzner, R., Shulakova, V., ... Lueth, S. (2013). Field testing of fiber-optic distributed acoustic sensing (das) for subsurface seismic monitoring. *The Leading Edge*, *32*, 593-724.

Daub, E. G., & Carlson, J. M. (2008). A constitutive model for fault gouge deformation in dynamic rupture simulations. *Journal of Geophysical Research*, *113*, 1-19.

Detournay, E. (2004). Propagation regimes of fluid-driven fractures in impermeable rocks. *International Journal of Geomechanics*, *4*, 35-45.

Dieterich, J. (1994). A constitutive law for rate of earthquake production and its application to earthquake clustering. *Journal of Geophysical Research*, *99*, 2601-2618.

Dieterich, J., Cayol, V., & Okubo, P. (2000). The use of earthquake rate changes as a stress meter at kilauea volcano. *Nature*, *408*, 457-460.
Dieterich, J., & Kilgore, B. D. (1994). Direct observations of frictional contacts: New insights for state-dependent properties. *Pure and Applied Geophysics*, *143*, 283-302.
Drew, J., White, R. S., Tilmann, F., & Tarasewicz, J. (2013). Coalescence microseismic mapping. *Geophysical Journal International*, *195*, 1773-1785.
Dvorak, J. J., Okamura, A. T., English, T. T., Koyanagi, R. Y., Nakata, J. S., Sako, M. K., … Yamashita, K. M. (1986). Mechanical response of the south flank of kilauea volcano, hawaii, to intrusive events along the rift systems. *Tectonophysics*, *124*, 193-209.
Eaton, D. W. (2018). *Passive seismic monitoring of induced seismicity.* Cambridge: Cambridge University Press.
Frohlich, C., DeShon, H., Stump, B., Hayward, C., Hornbach, M., & Walter, J. I. (2016). A historical review of induced earthquakes in texas. *Seismological Research Letters*, *87*, 1-17.
Gangi, A. F. (1970). A derivation of the seismic representation theorem using reciprocity. *Journal of Geophysical Research*, *75*, 2088-2095.
Gordeliy, E., & Peirce, A. (2013). Implicit level set schemes for modeling hydraulic fractures using the xfem. *Computer Methods in Applied Mechanical Engineering*, *266*, 125-143.
Grechka, V., Li, Z., Howell, B., Garcia, H., & Wooltorton, T. (2017). High-resolution microseismic imaging. *The Leading Edge*, *October*, 822-828.
Guglielmi, Y., Cappa, F., Avouac, J. P., Henry, P., & Elsworth, D. (2015). Seismicity triggered by fluid injection-induced aseismic slip. *Science*, *348*, 1224-1226.
Guglielmi, Y., Elsworth, D., Cappa, F., Henry, P., Gout, C., Dick, P., & Durand, J. (2015). In situ observations on the coupling between hydraulic diffusivity and displacements during fault reactivation in shales. *Journal de Physique*, *120*, 7729-7748.
Hakimhashemi, A., Schoenball, M., Heidback, O., Zhang, A., & Grunthal, G. (2014). Forward modelling of seismicity rate changes in georeservoirs with a hybrid geomechanical-statistical prototype model. *Geothermics*, *52*, 185-194.
Hamling, I. J., Wright, T. J., Calais, E., Bennati, L., & Lewi, E. (2010). Stress transfer between thirteen successive intrusions in ethiopia. *Nature Geoscience Letters*, *3*, 713-717.
Harris, R. A., & Simpson, R. W. (1998). Suppresion of large earthquakes by stress shadows: A comparison of coulomb and rate-and-state failure. *Journal of Geophysical Research*, *103*, 24439-24451.
Heimisson, E. R., & Segall, P. (2018). Constitutive law for earthquake production based on rate-and-state friction: Dieterich 1994 revisited. *Journal of Geophysical Research*, *123*, 1-16.
Hoek, E., & Martin, C. D. (2014). Fracture initiation and propagation in intact rock - a review. *Journal of Rock Mechanics and Geotechnical Engineering*, *6*, 287-300.
Ince, E. L. (1956). *Ordinary differential equations.* New York: Dover Publications.
Johnson, D. L., Koplik, J., & Dashen, R. (1987). Theory of dynamic permeability and tortuosity in fluid-saturated porous media. *Journal of Fluid Mechanics*, *176*, 379-402.
Johnson, L. R., & Majer, E. L. (2017). Induced and triggered earthquakes at the geysers geothermal field. *Geophysical Journal International*, *209*, 1221-1238.
Kagan, Y. Y., & Jackson, D. D. (2016). Earthquake rate and magnitude distributions of great earthquakes for use in global forecasts. *Geophysical Journal International*, *206*, 630-643.
Karpfinger, F., Muller, T. M., & Gurevich, B. (2009). Green's functions and radiation patterns in poroelastic solids revisited. *Geophysical Journal International*,

178, 327-337.
Kennett, B. L. N. (1983). *Seismic wave propagation in a stratified medium.* Cambridge: Cambridge University Press.
Kroll, K. A., Richards-Dinger, K. B., Dieterich, J. H., & Cochran, E. S. (2017). Delayed seismicity rate changes controlled by static stress transfer. *Journal of Geophysical Research*, *122*, 7951-7965.
Masson, Y. J., & Pride, S. R. (2010). Finite-difference modeling of biot's poroelastic equations across all frequencies. *Geophysics*, *75*, N33-N41.
Masson, Y. J., & Pride, S. R. (2011). Seismic attenuation due to patchy saturation. *Journal of Geophysical Research*, *116*, 1-17.
Masson, Y. J., Pride, S. R., & Nihei, K. T. (2006). Finite difference modeling of biot's poroelastic equations at seismic frequencies. *Journal of Geophysical Research*, *111*, 1-13.
McClain, W. C. (1971). *Seismic mapping of hydraulic fractures* (Technical Report No. ORNL-TM-3502). Oak Ridge National Laboratory.
Norris, A. N. (1994). Dynamic green's functions in anisotropic piezoelectric, thermoelastic and poroelastic solids. *Proceedings of the Royal Society of London, A*, *447*, 175-188.
Paige, C. C., & Saunders, M. A. (1982). Lsqr: An algorithm for sparse linear equations and sparse linear systems. *ACM Trans. Math. Software*, *8*, 195-209.
Passarelli, L., Mccaferri, F., Rivalta, E., Dahm, T., & Abebe Boku, E. (2013). A probabilistic approach to the classification of earthquakes as 'triggered' or 'not triggered'. *Journal of Seismology*, *17*, 165-187.
Pedersen, R., Sigmundsson, F., & Einarsson, P. (2007). Controlling factors on earthquake swarms associated with magmatic intrusions; constraints from iceland. *Journal of Volcanology and Geothermal Research*, *162*, 73-80.
Picklands, J. I. (1975). Statistical inference using extreme order statistics. *Annuals of Statistics*, *3*, 119-131.
Pozdniakov, S., & Tang, C.-F. (2004). A self-onsistent approach for calculating the effective hydraulic conductivity of a binary, heterogeneous medium. *Water Resources Research*, *40*, 1-13.
Pride, S. R. (2005). Relationships between seismic and hydrological properties. In *Hydrogeophysics* (p. 253-291). Springer, New York: p.
Pride, S. R., Berryman, J. G., Commer, M., Nakagawa, S., Newman, G. A., & Vasco, D. W. (2016). Changes in geophysical properties caused by fluid injection into porous rocks: analytical models. *Geophysical Prospecting*, 1-25. doi: 10.1111/1365-2478.12435
Pride, S. R., & Haartsen, M. W. (1996). Electroseismic wave properties. *Journal of the Acoustical Society of America*, *100*, 1301-1315.
Rice, J. R., & Cleary, M. P. (1976). Some basic stress diffusion solutions for fluid-saturated elastic porous media with compressible constituents. *Reviews of Geophysics and Space Physics*, *14*, 227-241.
Rozhko, A. Y. (2010). Role of seepage forces on seismicity triggering. *Journal of Geophysical Research*, *115*, 1-12.
Rutledge, J. T., & Phillips, W. S. (2003). Hydraulic stimulation of natural fractures as revealed by induced microearthquakes, carthage cotton valley gas field, east texas. *Geophysics*, *68*, 441-452.
Rutqvist, J., Birkholzer, J., & Tsang, C.-F. (2008). Coupled reservoir geomechanical analysis of the potential for tensile and shear failure associated with co_2 injection in multilayered reservoir caprock systems. *International Journal iof Rock Mechanics and Mining Science*, *45*, 132-143.
Rutqvist, J., Rinaldi, A., Cappa, F., & Moridis, G. J. (2013). Modeling of fault reactivation and induced seismicity during hydraulic fracturing of shale-gas reservoirs. *Journal of Petroleum Science and Engineering*, *107*, 31-44.
Segall, P. (1989). Earthquakes triggered by fluid extraction. *Geology*, *17*, 942-946.

Segall, P., & Lu, S. (2015). Injection-induced seismicity: Poroelastic and earthquake nucleation effects. *Journal of Geophysical Research*, *120*, 5082-5103.

Shapiro, S. A., Rothert, E., Rath, V., & Rindschwentner, J. (2002). Characterization of fluid transport properties of reservoirs using induced microseismicity. *Geophysics*, *67*, 212-220.

Shelly, D. R., Hill, D. P., Massin, F., Farrell, J., Smith, R. B., & Taira, T. (2013). A fluid-driven earthquake swarm on the margin of the yellowstone caldera. *Journal of Geophysical Research*, *118*, 1-15. doi: 10.1002/jgrb.50362

Snee, J.-E. L., & Zoback, M. D. (2016). State of stress in texas: Implications for induced seismicity. *Geophysical Research Letters*, *43*, 10208-10214. doi: 10.1002/2016GL070974

Stein, R. S. (1999). The role of stress transfer in earthquake occurrence. *Nature*, *402*, 605-609.

Tary, J. B., van der Baan, M., & Eaton, D. W. (2014). Interpretation of resonance frequencies recorded during hydraulic fractureing treatments. *Journal of Geophysical Research*, *119*, 1295-1315.

Terakawa, T., & Matsu'ura, M. (2008). Cmt data inversion using a bayesian information criterion to estimate seismogenic stress fields. *Geophysical Journal International*, *172*, 674-685.

Vasco, D. W., Alfi, M., Hosseini, S. A., Zhang, R., Deley, T., Ajo-Franklin, J. B., & Hovorka, S. D. (2019). The seismic response to injected carbon dioxide: Comparing observations to estimates based upon fluid flow modeling. *Journal of Geophysical Research*, *124*, 6880-6907.

Vasco, D. W., Nakagawa, S., Petrov, P., & Newman, G. (2019). Rapid estimation of earthquake locations using waveform traveltimes. *Geophysical Journal International*, *217*, 1727-1741.

Wang, H. F. (2000). *Theory of linear poroelasticity.* Princeton: Princeton University Press.

Wenzel, F. (2017). Fluid-induced seismicity: comparison of rate- and state- and critical pressure theory. *Geothermal Energy*, *5*, 1-16.

Wynants-Morel, N., Cappa, F., De Barros, L., & Ampuero, J. P. (2020). Stress perturbationns from aseismic slip drives the seismic front during fluid injection in a permeable fault. *Journal of Geophysical Research*, *125*, 1-23.

Yarushina, V. M., Bercovici, D., & Oristaglio, M. L. (2013). Rock deformation models and fluid leak-off in hydraulic fracturing. *Geophysical Journal International*, *194*, 1514-1526.

Zhai, G., & Shirzaei, M. (2018). Fluid injection and time-dependent seisimic hazard in the barnett shale, texas. *Geophysical Research Letters*, *45*, 4743-4753.

Zhang, C.-C., Shi, B., Zhu, H.-H., Wang, B.-J., & Wei, G.-Q. (2020). Toward distributed fiber-optic sensing of subsurface deformation: A theoretical quantification of ground-borehole interaction. *Journal of Geophysical Research*, *125*, 1-25.

Zhou, X., & Burbey, T. J. (2014). Fluid effects on hydraulic fracture propagation behavior: a comparison between water and supercritical co_2-like fluid. *Geofluids*, *14*, 174-188.